Journal of Colloid and Interface Science 675 (2024) 236–250

Contents lists available at ScienceDirect

Journal of Colloid And Interface Science

journal homepage: www.elsevier.com/locate/jcis

Regular Article

Enhancing colloidal stability of nanodiamond via surface modification with dendritic molecules for optical sensing in physiological environments

Maciej J. Głowacki [a,*,1], Paweł Niedziałkowski [b], Jacek Ryl [c], Marta Prześniak-Welenc [c], Mirosław Sawczak [d], Klaudia Prusik [c], Mateusz Ficek [a], Monika Janik [e], Krzysztof Pyrchla [a], Michał Olewniczak [f], Krzysztof Bojarski [f], Jacek Czub [f], Robert Bogdanowicz [a,*]

[a] Gdańsk University of Technology, Faculty of Electronics, Telecommunications and Informatics, Department of Metrology and Optoelectronics, Narutowicza 11/12, 80-233 Gdańsk, Poland
[b] University of Gdańsk, Faculty of Chemistry, Department of Analytical Chemistry, Wita Stwosza 63, 80-308 Gdańsk, Poland
[c] Gdańsk University of Technology, Faculty of Applied Physics and Mathematics, Institute of Nanotechnology and Materials Engineering, Narutowicza 11/12, 80-233 Gdańsk, Poland
[d] Polish Academy of Sciences, The Szewalski Institute of Fluid-Flow Machinery, The Centre for Plasma and Laser Engineering, Fiszera 14, 80-231 Gdańsk, Poland
[e] Warsaw University of Technology, Institute of Microelectronics and Optoelectronics, Koszykowa 75, 00-662 Warsaw, Poland
[f] Gdańsk University of Technology, Faculty of Chemistry, Department of Physical Chemistry, Narutowicza 11/12, 80-233 Gdańsk, Poland

GRAPHICAL ABSTRACT

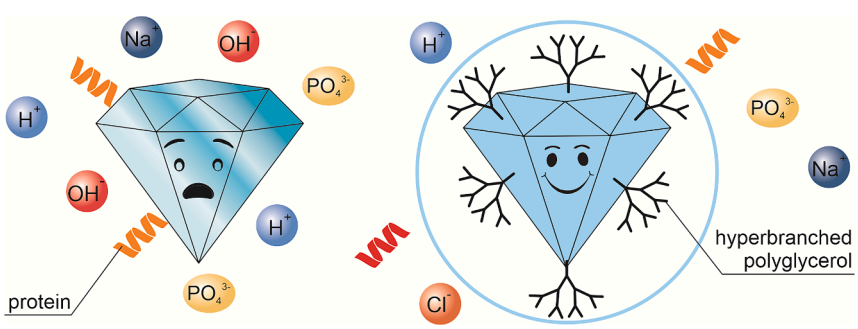

ARTICLE INFO

Keywords:
Nanodiamonds
Hyperbranched polyglycerol
Colloidal stability
Optical sensing
Nonspecific protein adsorption
Molecular dynamics

ABSTRACT

Pre-treatment of diamond surface in low-temperature plasma for oxygenation and in acids for carboxylation was hypothesized to promote the branching density of the hyperbranched glycidol polymer. This was expected to increase the homogeneity of the branching level and suppress interactions with proteins. As a result, composite nanodiamonds with reduced hydrodynamic diameters that are maintained in physiological environments were anticipated. Surfaces of 140-nm-sized nanodiamonds were functionalized with oxygen and carboxyl groups for grafting of hyperbranched dendritic polyglycerol via anionic ring-opening polymerization of glycidol. The modification was verified with Fourier-transform infrared spectroscopy and X-ray photoelectron spectroscopy. Dynamic light scattering investigated colloidal stability in pH-diverse (2–12) solutions, concentrated phosphate-buffered saline, and cell culture media. Thermogravimetric analysis of nanodiamonds-protein incubations

* Corresponding authors.
E-mail addresses: maciej-jerzy.glowacki@oc.uni-stuttgart.de (M.J. Głowacki), rbogdan@eti.pg.edu.pl (R. Bogdanowicz).
[1] Current affiliation: University of Stuttgart, Faculty of Chemistry, Institute of Organic Chemistry, Pfaffenwaldring 55, 70569 Stuttgart.

https://doi.org/10.1016/j.jcis.2024.06.225
Received 15 April 2024; Received in revised form 17 June 2024; Accepted 28 June 2024
Available online 28 June 2024
0021-9797/© 2024 The Authors. Published by Elsevier Inc. This is an open access article under the CC BY license (http://creativecommons.org/licenses/by/4.0/).

examined non-specific binding. Fluorescence emission was tested across pH conditions. Molecular dynamics simulations modeled interparticle interactions in ionic solutions. The hyperbranched polyglycerol grafting increased colloidal stability of nanodiamonds across diverse pH, high ionic media like 10 × concentrated phosphate-buffered saline, and physiological media like serum and cell culture medium. The hyperbranched polyglycerol suppressed non-specific protein adsorption while maintaining intensive fluorescence of nanodiamonds regardless of pH. Molecular modelling indicated reduced interparticle interactions in ionic solutions correlating with the improved colloidal stability.

1. Introduction

Fluorescent nanodiamonds (NDs) are recognized as an attractive platform for optical detection within physiological media. Their applications in live cells include, but are not limited to, magnetic-based orientation tracking [1], cell labeling and targeting [2], monitoring of cellular uptake [3] and temperature measurements with sub-Kelvin sensitivity [4]. Although the cores of NDs are chemically inert [5], their untreated surfaces carry a vast range of moieties, which induce a net charge that spontaneously attracts selected proteins present in physiological environments. Coating of surfaces of NDs with a protein corona, combined with the negative effect of salts on colloidal stability of these particles, results in a significant aggregation [6]. This aggregation impairs their effectiveness as sensors or gene carriers, limiting the practical utility of NDs. To address this critical issue, various advanced surface modification techniques are employed to prepare the surfaces of NDs before exposure to physiological media to guarantee their satisfactory colloidal stability.

Takimoto et al. [7] exploited multistep process of organic synthesis to covalently coat NDs (30 nm in size) produced by high-pressure high-temperature (HPHT) method with polyethylene glycol and fluorescein to create particles which retain stability in phosphate-buffered saline (PBS) for over a month. Kulvelis et al. [8] combined two water-based liquids – a suspension of NDs (4.5 nm in size) produced by detonation (DNDs) and a solution of polyvinylpyrrolidone – to create complexes maintaining colloidal stability in pH range from 2.0 to 11.5, in PBS and saline solution. Merz et al. [9] developed an elaborate surface modification of milled DNDs (≈ 3.5 nm peak particle size in volume-weighed distribution) using benzoic acid, alkane thiolate, tetraethylene glycol and zwitterionic head groups to prevent the development of hard protein corona. The modified NDs were stably suspended in mixtures of water and physiological media – Fetal Bovine Serum (FBS), Dulbecco's Modified Eagle Medium (DMEM) – for a minimum of 7 days.

Due to its excellent biocompatibility, chemical stability, high water-solubility and a resistance to nonspecific adsorption of proteins [10,11], hyperbranched polyglycerol (HPG) has been frequently used to modify surfaces of carbon-based nanomaterials, including graphene and graphene oxide, carbon nanotubes, fullerenes, carbon dots and carbon fibers [12]. Since 2011 [13], HPG has been increasingly used to modify surfaces of NDs aimed to function in physiological media [12]. The high hydrophilicity of HPG is induced by its peripheral hydroxyl groups, which are easily addressed chemically, making it possible to perform further functionalizations [10,13,14]. Compared to polymers that form linear chains (like polyethylene glycol), HPG may be conjugated to surfaces of particles substantially more thickly [13]. The other advantages of HPG over polyethylene glycol are the greater number of hydroxyl groups, resulting in higher hydrophilicity, as well as the larger surface area [12]. Contrary to structurally akin dendrimers, HPG is synthesized using simpler methods, though its structure is notably more disordered, with broader distribution of molecular weights, lower degree of branching, and more random allocation of functional groups [11,15].

Zhao et al. polymerized HPG on NDs (sizes of 30 nm [13] and 50 nm [16]) produced by HPHT method through neutral ring-opening polymerization (ROP) of glycidol performed at high temperature (140 °C). Suspensions of the resulting HPG-modified NDs [13] in water, methanol, PBS, and phosphate buffer with addition of sodium sulfate exhibited colloidal stability. Boudou et al. [14] conjugated fluorescent NDs (average size of ≈30 nm) obtained by HPHT technique with HPG in a catalyst-free, high-temperature, neutral ROP of glycidol, and suspended the resulting particles in 1 M solution of sodium chloride in water. After centrifugation at 4500 g for 5 min, the suspension showed negligible precipitation. HPG-modified NDs produced by Sotoma et al. [17] (median size of 53 nm prior to modification) were found to stay well-dispersed in PBS for at least 2 h. HPG prevented lysozyme from nonspecific adsorption to the modified particles. A subsequent attachment of a monoclonal antibody to HPG-modified NDs made it possible to carry out specific targeting of an epidermal growth factor receptor on live cells. Huang et al. [18] coated DNDs (diameters from 2 to 10 nm) with adamantine, while separately synthesizing HPG on β-Cyclodextrin using anionic ROP of glycidol. The adamantine and β-Cyclodextrin were combined into complexes via host–guest interactions, thus producing HPG-modified NDs, which showed increased dispersibility in water and reduced toxicity towards A549 cells. Terada et al. [19] coated carboxylated, fluorescent NDs (sizes of 50 nm and 100 nm) produced by HPHT method with a thin layer (thickness of 5 nm and 16 nm, respectively) of HPG terminated with carboxyl groups. HPG provided the NDs with colloidal stability in PBS for at least 2 h and prevented nonspecific adsorption of HeLa cells components to the surfaces of the particles. Moreover, carboxyl-terminated HPG was further conjugated with a range of molecules, including biotin derivatives, anti-integrin β3 monoclonal antibody, and mitochondrial localization signal peptides. Maziukiewicz et al. [20] conjugated fluorescent NDs (4–5 nm individual grains, aggregated into > 2 μm clusters) produced by liquid-phase pulsed laser ablation with HPG via high-temperature, neutral ROP of glycidol, and afterwards coated the particles with polydopamine. The resulting, composite particles showed substantially reduced hydrodynamic diameters, which were maintained for at least a week following their dispersion in PBS, saline buffer or cell medium.

The primary aim of this study was to enhance the colloidal stability of NDs in physiological environments through surface modification with HPG, while retaining their intrinsic fluorescence for effective optical detection within variable cellular contexts. Development of a surface modification that does not hinder the optical addressability of NDs and ensures a stable level of their fluorescence, while providing the particles with excellent colloidal stability regardless of their dispersion medium, could substantially contribute to the engineering of versatile biomarkers for tailored applications in optical detection within cellular environments characterized by variable pH or contents of proteins/salts. Prior to the modification, surfaces of the particles were homogenized and saturated with oxygen-containing functional groups, which served as surface sites for the polymerization of HPG chains [13,14] during the anionic ROP of glycidol [10]. Fourier-transform infrared (FTIR) spectroscopy and X-ray photoelectron spectroscopy (XPS) were employed to verify the outcome of the modification process. The dispersibility and colloidal stability of HPG-modified NDs suspended in pH-diverse (2.00–12.00) aqueous solutions, in highly ionic environment (10 × concentrated PBS) and physiological media (FBS, DMEM) were investigated using dynamic light scattering (DLS). Non-modified and HPG-modified NDs incubated in FBS and DMEM were additionally subjected to thermogravimetric analysis (TGA) to investigate the effect of HPG on nonspecific adsorption of proteins. Furthermore, fluorescence emission of the particles in

MOST WIEDZY

relation to pH of the surrounding environment was examined. Finally, to gain perspective on the interparticle interactions between non-modified and HPG-modified NDs suspended in the highly ionic environment, a series of molecular dynamics (MD) simulations was performed. Unlike previous studies, this work incorporates a comprehensive array of analytical techniques, revealing the mechanisms influencing diamond interaction processes. The results collectively highlight the efficiency of presented surface modification approach and demonstrate its superior performance in environments with high ionic strength and abundant proteins.

2. Experimental

2.1. Materials

NDs produced by HPHT procedure were commercially obtained from Pureon AG (Switzerland; '*MSY 0–0.25 μm*') and supplied in powder form. These particles were used as starting NDs for the modification process. Size distributions of the starting NDs upon their dispersion in deionized water are presented in Fig. 1a. According to the volume-weighed distribution, the particles are characterized by a peak hydrodynamic diameter of 142 nm, and the vast majority of the NDs (between the 10th and 90th percentile) falls between 78 nm and 183 nm. Fig. 1b shows SEM image of the starting NDs drop-cast on a silicon substrate. The image reveals nonspherical, ≈140 nm-sized particles with irregular, sharp edges, typical for NDs produced by HPHT process. The particles are gathered together as a result of drying.

Glycidol was obtained from Sigma-Aldrich (Germany). Toluene and anhydrous methanol were purchased from POCH (Poland). Sulfuric acid H_2SO_4, sodium hydroxide NaOH, and hydrochloric acid HCl were all acquired from Chempur (Poland). Nitric acid HNO_3 was obtained from STANLAB (Poland). PBS tablets (OmniPur) were purchased from Sigma-Aldrich (Germany). Gibco Fetal Bovine Serum and Gibco Dulbecco's Modified Eagle Medium were acquired from Thermo Fisher Scientific. Deionized water was produced from municipal water using the HLP Smart water purification system (Hydrolab, Poland).

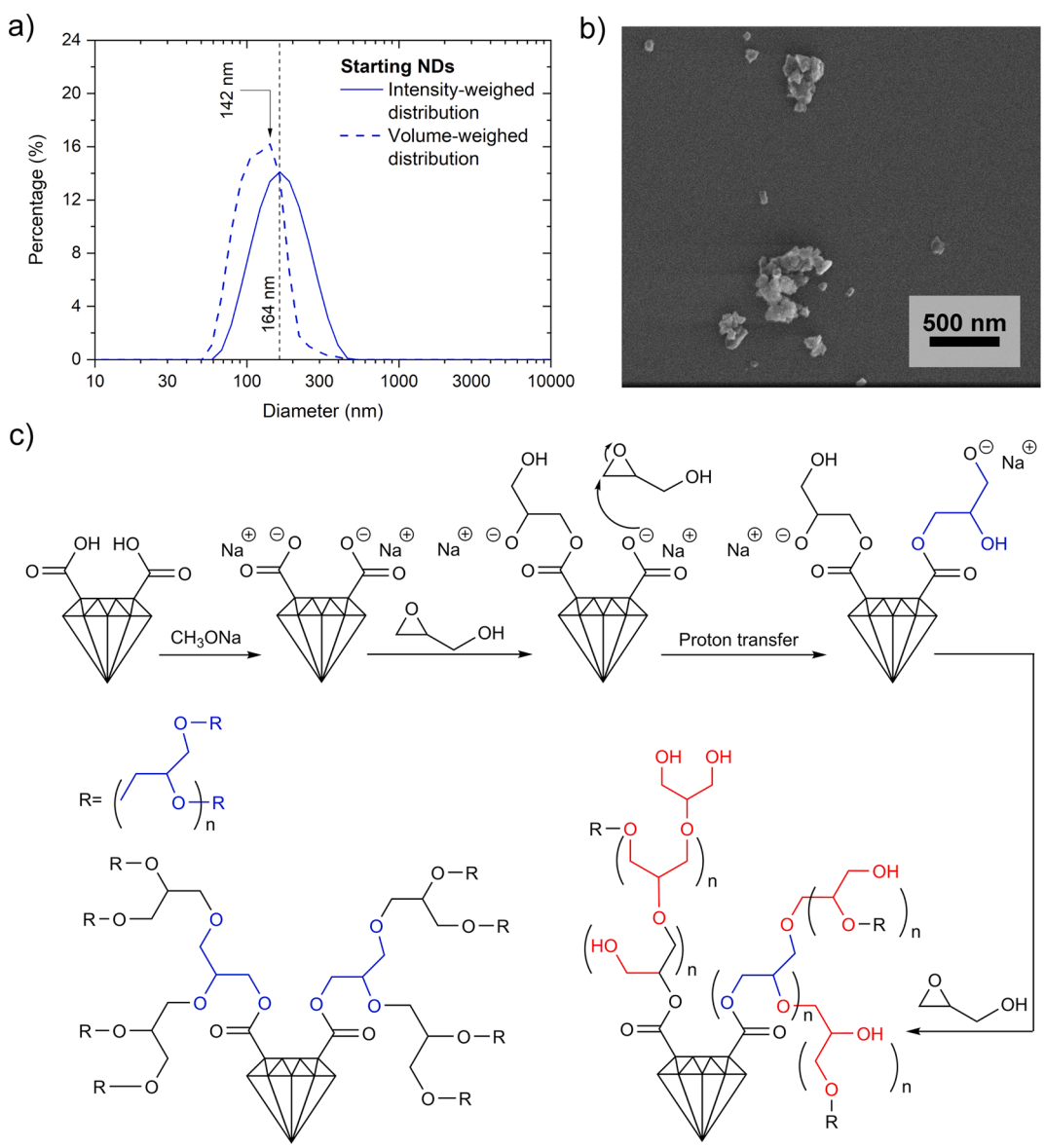

Fig. 1. a) Intensity- and volume-weighed size distribution of the starting NDs (*'MSY 0–0.25 μm'* by Pureon AG, Switzerland) dispersed in deionized water; the results were averaged from 5 consecutive measurements; b) SEM image of the starting NDs drop-cast on a silicon substrate; c) Scheme of the chemical modification of NDs with HPG.

MOST WIEDZY

2.2. Functionalization of NDs with oxygen-containing groups

Two different types of treatment – oxygenation in plasma or carboxylation in acids – were performed on separate portions of the starting NDs to generate large numbers of oxygen-containing functional groups on their surfaces. To oxygenate the particles in plasma, a ZEPTO low-pressure plasma cleaner (Diener Electronic, Germany) was used. The starting NDs were spread across glass Petri dishes and introduced into a chamber of the cleaner. After the air was pumped out of the chamber, the oxygen was introduced and the radiofrequency (13.56 MHz) plasma was generated at 0.3 mbar pressure and 300 W power. The particles were subjected to the plasma for 10 min. The resulting, oxygenated NDs were labeled **NDs-O**.

The mixed acid carboxylation [21,22] began by suspending the starting NDs in a 1:1 (v:v) mixture of H_2SO_4 and HNO_3 (without dilution). After the suspension was magnetically stirred for 48 h at 75 °C, the NDs were moved to a 0.1 M solution of NaOH in deionized water and stirred for additional 2 h at 90 °C. Next, the NDs were suspended in a 0.1 M solution of HCl in deionized water and further stirred for 2 h at 90 °C. The solid product was repeatedly washed with deionized water, centrifuged at 10,000 RPM for 30 min using an MPW-201 centrifuge (Mechanika Precyzyjna, Poland) and finally dried. The resulting, acid-carboxylated NDs were labeled **NDs-C**.

2.3. Modification of oxygen-terminated NDs with HPG

HPG was polymerized on the surfaces of the oxygen-terminated NDs via anionic ROP of glycidol [10,23] using a procedure schematically depicted in Fig. 1c. The same preparative procedure was performed separately for **NDs-O** and **NDs-C** particles. In the first step, deprotonation of NDs was performed using sodium methoxide. For this purpose, 10 mL of freshly prepared 2 M of sodium methoxide was added to a round-bottom flask containing previously lyophilized NDs (100 mg). Then, the suspension was homogenized in a Sonorex ultrasonic bath (Bandelin, Germany) at 35 kHz for 30 min. Next, the flask equipped with a reflux condenser fitted with a $CaCl_2$ drying tube was stirred on a magnetic stirrer in an oil bath for 17 h at 70 °C. After cooling to room temperature, the NDs were centrifuged at 6000 RPM for 10 min and washed with 10 mL of anhydrous methanol. Then, 5 repetitions of a process consisting of 10-minute sonication in the ultrasonic bath, followed by washing with 10 mL of anhydrous methanol and centrifugation at 6000 RPM for 5 min, were carried out. Then, the deprotonated NDs were dried in vacuum under P_2O_5 for 24 h.

In the second step, 11 mL of toluene and 3 mL of glycidol were added to the previously deprotonated NDs, and the resulting suspension was homogenized in the ultrasonic bath for 1 h. The reaction mixture was stirred in the oil bath for 18 h at 100 °C. After the reaction was completed, the liquid layer was removed and the obtained, HPG-modified NDs were washed with 10 mL of anhydrous methanol, and the suspension was homogenized in the ultrasonic bath for 10 min and centrifuged at 6000 RPM for 5 min. The procedure of washing with anhydrous methanol was performed 3 more times, and finally, water was used to wash the obtained HPG polymerized on the surfaces of NDs, which were dried in vacuum under P_2O_5 for 24 h. After the modification, the particles (labeled **NDs-O-HPG** for NDs previously plasma-oxygenated, and **NDs-C-HPG** for NDs previously acid-carboxylated) were examined by means of FTIR and XPS.

2.4. Evaluation of colloidal stability of HPG-modified NDs

To verify the effect of pH of a liquid on the colloidal stability of non-modified (reference) and HPG-modified NDs dispersed in the liquid, a series of aqueous dispersion media, characterized by eleven integer pH values ranging from 2.00 to 12.00, was prepared by adding either 0.1 M HCl or 0.1 M NaOH to deionized water. The acid was added to create dispersion media with resulting pH of 2.00–6.00, while the hydroxide was introduced to prepare media characterized by the resulting pH of 7.00–12.00. The compounds were added to water gradually to achieve desired values of pH, which were observed in real time with a SevenCompact S210 pH meter fitted with the InLab Expert Pro-ISM electrode (Mettler-Toledo, Poland).

Aqueous suspensions of oxygen-terminated NDs (**NDs-O** and **NDs-C**) and HPG-modified NDs (**NDs-O-HPG** and **NDs-C-HPG**) were prepared by dispersing the respective particles (in dried powder state) in deionized water to obtain 10 mg/mL concentrations. These aqueous suspensions were vortexed for 5 min at 2500 RPM with a TX4 digital vortex mixer (VELP Scientifica, Italy). The suspensions were further homogenized in a Sonic-3 ultrasonic bath (Polsonic, Poland) for 45 min before mixing portions (100 μL) of each of them with portions (9.9 mL) of each of the eleven dispersion media with varied pH, thus yielding nanodiamond suspensions with 100 μg/mL concentrations of the particles and pH levels covering a broad range. The resulting suspensions were vortexed for additional 30 sec at 2500 RPM, after which their particle size distributions, zeta potentials, and fluorescence were inspected.

To investigate if the introduction of NDs brings changes to pH values of the aqueous solutions of HCl or NaOH, small portions of the nanodiamond suspensions with varied pH levels (**NDs-O**, **NDs-C**, **NDs-O-HPG**, **NDs-C-HPG** at pH of 2.00–12.00) were subjected to centrifugation for 30 min at 10,000 RPM, and the resulting supernatants were examined for their pH. Removal of NDs from the liquids through centrifugation was performed to minimize the risk of the pores of the pH meter electrode becoming clogged with nanoparticles, which could negatively impact the accuracy of reported pH values.

To create 10 × concentrated PBS (1.37 M of NaCl, 0.027 M of KCl, 0.1 M of Na_2HPO_4), used as a dispersion medium to assess the dispersibility of NDs in an extreme ionic environment [24], two PBS tablets were dissolved per 20 mL of deionized water (1 × PBS is prepared by dissolving one tablet in 100 mL of water). Oxygen-terminated NDs (**NDs-O** and **NDs-C**) and HPG-modified NDs (**NDs-O-HPG** and **NDs-C-HPG**), suspended in deionized water (10 mg/mL), were introduced to 10 × concentrated PBS by adding 100 μL of the aqueous nanodiamond suspensions to 9.9 mL of the buffer solution and homogenizing the resulting mixtures in the ultrasonic bath for 15 min. Size distributions of all the NDs dispersed in the concentrated buffer were measured via DLS directly after the ultrasonic homogenization, 24 h later, and 48 h later. Additionally, size distributions of **NDs-O-HPG** and **NDs-C-HPG** particles were further examined after 1 week and 2 weeks.

2.5. Assessment of nonspecific protein adsorption to the surfaces of HPG-modified NDs

To verify if HPG present on the surfaces of modified NDs effectively inhibits nonspecific adsorption of proteins and the resulting development of soft and hard protein corona, dried powders of plasma-oxygenated (**NDs-O**), acid-carboxylated (**NDs-C**) and HPG-modified (**NDs-O-HPG** and **NDs-C-HPG**) particles were suspended at 6.7 mg/mL concentrations in cell culture media – FBS and DMEM – diluted (1:5 v:v) with deionized water. The resulting suspensions, labeled **NDs-O-FBS**, **NDs-O-DMEM** (plasma-oxygenated particles), **NDs-C-FBS**, **NDs-C-DMEM** (acid-carboxylated particles), **NDs-O-HPG-FBS**, **NDs-O-HPG-DMEM** (plasma-oxygenated, HPG-modified particles), **NDs-C-HPG-FBS** and **NDs-C-HPG-DMEM** (acid-carboxylated, HPG-modified particles), were treated in the ultrasonic bath for 45 min. Subsequently, NDs were incubated in the media for 1 h at 37 °C, after which the suspensions were analyzed with DLS for particle size distributions. After the measurements, the suspensions were centrifuged for 15 min at 10,000 RPM to clear out the proteins that had not adhered to the surfaces of NDs at all, or had bound to them weakly, forming the soft corona. The supernatants were disposed of, and the precipitants were washed with deionized water 3 times. In a single washing step, 6 mL of deionized water was added to each of the precipitants, then the samples were homogenized with the vortex (for 1 min at 2500 RPM) and in the ultrasonic bath (for

MOST WIEDZY

30 min), and the resulting aqueous suspensions were centrifuged for 15 min at 10,000 RPM, after which the supernatants were again disposed of. After the third execution of the washing step, each precipitant was resuspended in 1 mL of deionized water, and DLS measurements were performed again (Fig. S1 in the Supplementary Information). The amounts of proteins adsorbed to the surfaces of NDs, forming the hard corona, were quantified using TGA. To carry out the measurements, the aqueous suspensions of washed NDs were freeze-dried overnight. The analysis was performed on the particles unincubated in the media (dried **NDs-O**, **NDs-C**, **NDs-O-HPG** and **NDs-C-HPG**), as well as incubated in diluted FBS (dried **NDs-O-FBS**, **NDs-C-FBS**, **NDs-O-HPG-FBS** and **NDs-C-HPG-FBS**) and diluted DMEM (dried **NDs-O-DMEM**, **NDs-C-DMEM**, **NDs-O-HPG-DMEM** and **NDs-C-HPG-DMEM**).

2.6. Measurement techniques

Fourier-transform infrared spectra were recorded using an IFS 66 spectrometer (Bruker, USA). All the measurements were performed using KBr by pellets method. High-resolution X-ray photoelectron spectroscopy measurements were carried out with an Escalab 250Xi spectrometer (Thermo Fisher Scientific), using Al-Kα X-ray source with 250 μm spot size. The pass energy was 20 eV. Peaks were calibrated utilizing adventitious carbon C1s peak at 284.8 eV. The obtained spectra were deconvoluted into peaks characterized by between 20 % and 40 % of Lorentzian vs Gaussian peak shape. The full width at half maximum of each component was constrained to not exceed 2.2 eV. "Smart" type background was used, a feature implemented in the Avantage software. Surface morphologies of NDs were investigated with an FEI Quanta FEG 250 scanning electron microscope (SEM) using 30 kV beam accelerating voltage and a secondary electron Everhart-Thornley detector working in a high-vacuum mode (pressure of 10^{-4} Pa).

A Zetasizer Nano ZS particle analyzer (Malvern Panalytical, UK), fitted with a He-Ne laser (central wavelength of 632.8 nm, output power of 4 mW) and a narrowband filter, served to determine size distributions of NDs via DLS and to measure zeta potentials of the particles via electrophoretic light scattering (ELS). For DLS analysis, suspensions of NDs were contained in disposable, macro-volume cuvettes (4.5 mL; outer dimensions of 12 × 12 × 45 mm) made of polystyrene, and the measurements were performed at 25 °C in a backscatter configuration (scattered light collected at 173° in regard to the incident laser beam). Six iterations of each measurement were made. Results based on the intensity of scattered light – mean hydrodynamic diameters (d_H), calculated from the cumulants analysis, and intensity-weighed particle size distributions, derived from distribution analysis – were chosen to describe NDs and compare the suspensions among themselves. Intensity-based modes of analysis favor larger particles, and therefore are preferred for revealing the occurrence of aggregates. The other modes of presenting DLS data, i.e. volume- or number-weighed particle size distributions, are calculated from the primary, intensity-based data using the refractive index (n) and the extinction coefficient (k) of the solid material suspended in liquids. Since the values of n and k for modified and/or incubated NDs should differ from those for pristine NDs (n = 2.42; k = 0.0) [25], the volume- and number-weighed results were not taken into account in this study as being more susceptible to distortions. Standard deviations (σ) of mean hydrodynamic diameters (d_H) for each population of NDs were determined using the equation (1):

$$\sigma = d_H \times \sqrt{PDI} \quad (1)$$

where *PDI* represents polydispersity index [26] – a parameter resulting from the cumulants analysis. Making 6 repetitions of each DLS measurement made it possible to calculate standard errors of the mean. In ELS measurements, the suspensions were examined at 25 °C in standard, folded capillary cells (DTS1070) using forward scattering configuration (scattered light collected at 13° in regard to the incident laser beam). Each measurement was repeated 5 times.

Thermogravimetric analysis was performed using an STA 449 F1 Jupiter thermal analyzer (Netzsch, Germany) under a nitrogen atmosphere with a consistent flow rate of 60 mL min^{-1} for a three-step temperature program. In the initial stage, the temperature ranged from 40 °C to 137 °C, with a heating rate of 10 °C min^{-1}, followed by a 60-minute isotherm at 137 °C to eliminate water adsorbed to the surfaces of NDs. Subsequently, the temperature was increased from 137 °C to 900 °C with a heating rate of 5 °C min^{-1}. A constant sample mass of 5 ± 0.5 mg was maintained throughout the analysis.

Fluorescence of NDs suspended in pH-diverse aqueous solutions was measured using a laboratory-built system which utilizes a Millenia Nd:YAG SHG continuous-wave laser (Spectra-Physics, USA) emitting a 532 nm beam of 500 mW for excitation. The optical emission signal was analyzed by means of an SR303i 0.3 m monochromator (Andor, UK) equipped with 600 groove/mm grating, and recorded with a DH740 iCCD detector (Andor, UK). The suspensions under investigation were placed in a quartz cuvette and illuminated with a laser at 45° angle. Fluorescence signal was collected from the front side of the cuvette using a quartz lens and focused on the optical fiber of the spectrometer. To eliminate the laser radiation, an OG570 bandpass filter (Schott, Germany) was used in the detection path. Each suspension was measured 3 times. Fluorescence spectra of pure aqueous solutions with diverse pH values were separately acquired and later subtracted from the spectra of the corresponding nanodiamond suspensions as a background.

2.7. Molecular dynamics (MD) simulations

A system incorporating a nanodiamond (ND) slab measuring 3.5 × 3.5 × 1.5 nm and composed of approximately 3500 carbon atoms was constructed. The (1 0 0) or (1 1 1) surfaces were hydrogenated with around 400 hydrogen atoms. On one of these surfaces, either one or two HPG molecules were attached (generation 8; Fig. S2 in the Supplementary Information) via the carboxyl group. The resulting HPG-modified ND slab was made periodic in the x–y plane within a rectangular simulation box of approximately 3.5 × 3.5 × 10 nm, ensuring covalent linkage of carbon atoms across the periodic boundary. To replicate real-world conditions and maintain an ionic strength equivalent to 10 × concentrated PBS used in experiments, the system was solvated with approximately 2500 water molecules and NaCl at a concentration of 1.5 M (Fig. S3 in the Supplementary Information).

All MD simulations were conducted using Gromacs 2020 [27]. The CHARMM General Force Field (CGenFF) [28] was applied for ND, its HPG modification and ions. Bulk carbon atoms connected to four other carbons were assigned zero partial charge, and the reference values for bond and angle terms within ND were extracted from crystallographic data. Water molecules were described using the TIP3P model. The x and y dimensions of the simulation box were fixed to allow periodic bonds, while maintaining a constant pressure of 1 bar along the z direction (normal to the ND surface) using the Parrinello-Rahman algorithm [29] with a coupling constant of 2 ps. The temperature was held at 300 K using v-rescale [30] with a coupling constant of 0.1 ps. Electrostatic interactions were computed using the Particle Mesh Ewald (PME) [31] method, employing a cut-off radius of 1.2 nm and a Fourier grid spacing of 0.1 nm. Van der Waals interactions were determined with the Lennard-Jones potential and a cut-off radius of 1.2 nm, applying a switching function from a distance of 1 nm. The equations of motion were integrated using a leap-frog algorithm with a time step of 2 fs. Following initial minimization and MD-based equilibration, the systems were simulated for 500 ns.

To investigate the association of two ND slabs via (1 0 0) surfaces, in the presence or absence of HPG, free energy calculations through umbrella sampling molecular dynamics were conducted. The center-of-mass distance between the associating ND surfaces, defined as the external layers of carbon atoms, served as the reaction coordinate. For this purpose, two ND slabs, as described above, were positioned within a simulation box. To enable sampling of different distances between the

MOST WIEDZY

ND surfaces, the slabs were made non-periodic, and the dimensions of the box were extended by 1 nm in both the x and y directions, resulting in box dimensions of 4.5 × 4.5 × 15 nm. 17 equally spaced umbrella sampling windows were employed, covering a range of 0.5–4.5 nm along the reaction coordinate. Each window underwent a 1-μs simulation using a harmonic bias potential with a spring constant of 250 kJ mol^{-1} nm^{-2}. To replicate the association between larger surfaces in real-world scenarios, the parallel orientation of NDs was maintained throughout the umbrella sampling simulations with additional orientational restraints. The same procedure was applied to both non-modified and HPG-modified ND slabs. The unbiased free energy profiles were reconstructed using the weighted histogram analysis method [32].

3. Results and discussion

3.1. Surface morphology of HPG-modified NDs

FTIR spectra of starting NDs, oxygen-terminated NDs (**NDs-O** and **NDs-C**) and HPG-modified NDs (**NDs-O-HPG** and **NDs-C-HPG**) are presented in Fig. 2a. The spectra of **NDs-O** and **NDs-C** were compared with the spectrum of the reference, starting NDs to verify if oxygenation in plasma or carboxylation in acids makes it possible to homogenize surfaces of the particles and saturate them with oxygen-containing groups. Therefore, in these spectra the emphasis was put on identifying bands resulting from carbonyl (C═O) and hydroxyl (–OH) groups, which form carboxyl (–COOH) groups when linked to a single carbon atom. The wide band reaching its minimum at 3435 cm^{-1} results from the presence of hydroxyl groups contained in water molecules physisorbed to the surfaces of NDs [21,33,34]. These –OH groups do not contribute to the formation of carboxyl groups [14]. The band at 1786 cm^{-1} is an outcome of C═O groups stretching [35]. The band at 1624 cm^{-1} is attributed to bending vibrations of hydroxyl and carbonyl groups [33], and is known to shift towards higher wavenumbers when particle size decreases [21]. In-plane bending vibration of hydroxyl groups causes the band at 1400 cm^{-1} [36], while C—O—C bonds are manifested in the band at 1089 cm^{-1} [35].

In the spectrum of the starting NDs, the bands attributed to –OH groups are visibly more prominent than the bands stemmed from C═O groups. FTIR analysis of **NDs-O** and **NDs-C** did not reveal any new bands in comparison to the spectrum of the starting particles; however, the level of bands attributed to hydroxyl groups relative to the bands ascribed to carbonyl groups is noticeably equalized, which proves the effective homogenization of the surfaces of the particles.

FTIR spectra of NDs conjugated with HPG (both **NDs-O-HPG** and **NDs-C-HPG**) include a wide band reaching its minimum at 3370 cm^{-1}, which indicates stretching vibration of O—H bond [10,18]. Whereas the bands from the stretching vibration of hydroxyl groups are noticeable in both of the spectra, the band for **NDs-C-HPG** is more intense over the spectrum, which may suggest a higher concentration of hydroxyl groups in comparison with **NDs-O-HPG**. Bands in the wavenumber range of 3000–2800 cm^{-1}, which are more intense for **NDs-C-HPG**, are produced by the overlapping of C—H stretching of polyglycerol tails [10]. Asymmetric and symmetric vibration of CH_2 groups, which are formed in the skeleton of HPG developing on the surfaces of NDs during the modification reaction, correspond to the peaks at 2917 cm^{-1} and 2876 cm^{-1}, respectively [37]. The peak at 1624 cm^{-1}, present for both **NDs-O-HPG** and **NDs-C-HPG**, corresponds to the carbonyl groups. In the wavenumber span from 1500 cm^{-1} to 1000 cm^{-1}, the bands resulting from CH_2–O–CH_2 scissoring (1458 cm^{-1}), wagging (1340 cm^{-1}) and stretching modes (1067 cm^{-1}) are visible for both **NDs-O-HPG** and **NDs-C-HPG** [10]. FTIR spectra presented in Fig. 2a prove successful surface modification of **NDs-O-HPG** and **NDs-C-HPG** particles by covalent conjugation with HPG. The bands corresponding to HPG bonds absorb significantly stronger in the spectrum of **NDs-C-HPG** sample, which suggests that the particles carboxylated in acids are covered with HPG to a larger extent than the particles subjected to the oxygenation in plasma

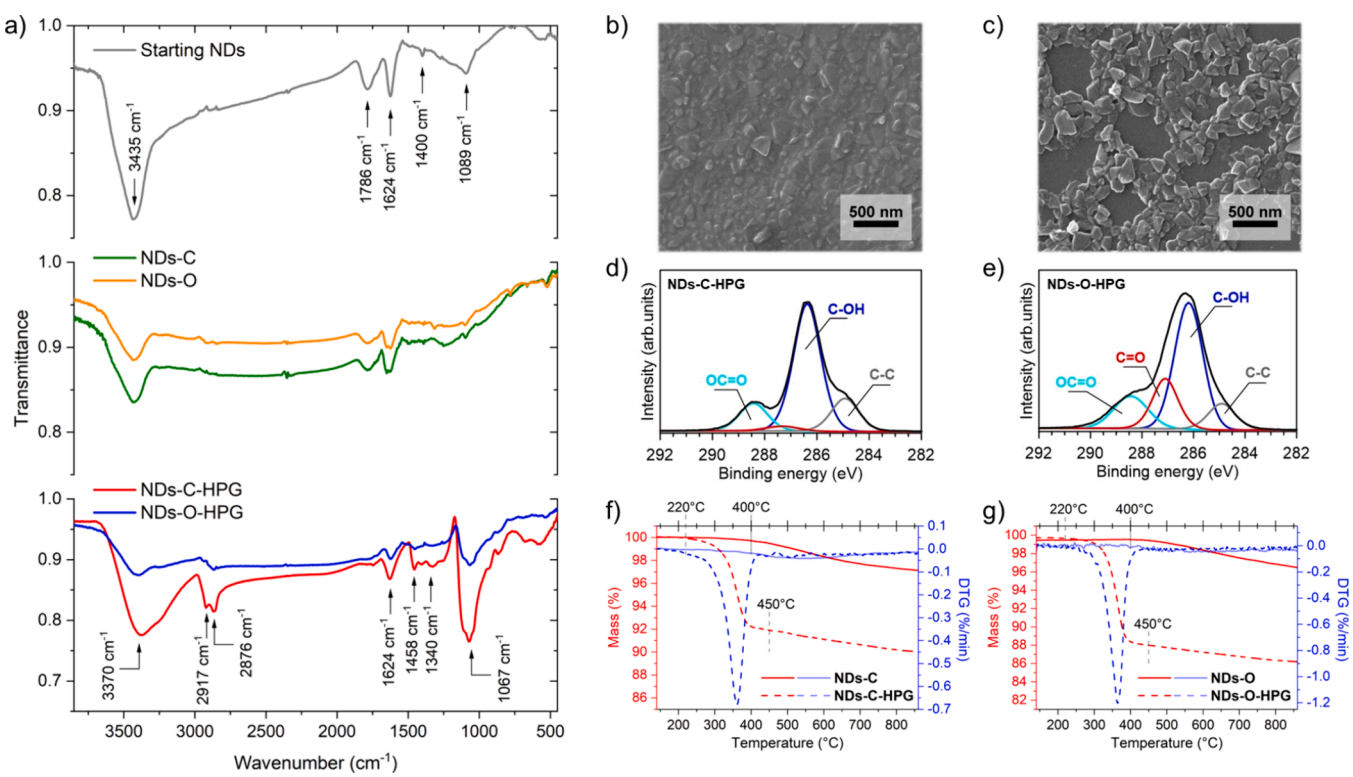

Fig. 2. a) FTIR spectra of starting NDs, oxygen-terminated NDs (**NDs-O** and **NDs-C**) and HPG-modified NDs (**NDs-O-HPG** and **NDs-C-HPG**); b) SEM image of acid-carboxylated NDs modified with HPG (**NDs-C-HPG**), deposited on a silicon substrate; c) SEM image of plasma-oxygenated NDs modified with HPG (**NDs-O-HPG**), deposited on a silicon substrate; d) high-resolution XPS C1s spectra of **NDs-C-HPG** particles; e) high-resolution XPS C1s spectra of **NDs-O-HPG** particles; f) thermogravimetric (TG) and derivative thermogravimetric (DTG) curves of **NDs-C** and **NDs-C-HPG**; g) TG and DTG curves of **NDs-O** and **NDs-O-HPG.**

MOST WIEDZY

(**NDs-O-HPG**).

SEM images of **NDs-C-HPG** and **NDs-O-HPG** particles drop-cast on silicon plates are presented in Fig. 2b and Fig. 2c, respectively. The images reveal that HPG polymerizes to a much larger degree on the surfaces of NDs subjected to mixed acid carboxylation (**NDs-C-HPG**, Fig. 2b) than particles exposed to the oxygen plasma (**NDs-O-HPG**, Fig. 2c). **NDs-C-HPG** are coated with a very thick layer of HPG, which encapsulates the particles entirely (Fig. 2b). Once the particles are brought together as a result of the solvent evaporation, the adjacent HPG coatings overlap, giving the effect of the particles being immersed in the hyperbranched polymer. In the SEM image of **NDs-O-HPG** (Fig. 2c), individual particles could be distinguished due to substantially thinner coating of the NDs with HPG. The successful coverage is still evident as **NDs-O-HPG** particles are characterized by rounded edges, which present a charging effect due to the nonconductive nature of HPG.

High-resolution XPS spectra recorded in the core-level C1s binding energy range, presented in Fig. 2d and Fig. 2e, make it possible to discuss surface chemistry of NDs. The spectra can be deconvoluted into four separate components. Binding energy positions, surface areas and full width at half maxima of the components are presented in Table S1 in the Supplementary Information. Two dominant peaks, located at approx 286.3 eV and 288.3 eV, testify the presence of hydroxyl and carboxyl bonds, confirming successful modification with HPG for both studied surface terminations [38,39]. Their share in total [C] content is approx. 79.8 % and 69.6 % for **NDs-C-HPG** and **NDs-O-HPG**, respectively. Notably, additional C1s peak appears at 287.3 eV and nearly exclusively for **NDs-O-HPG** (19.3 % total [C], compared to only 2.8 % for **NDs-C-HPG**), which is a result of carbonyl bonds formation due to plasma-oxygenation treatment [40,41]. Finally, the C—C peak located at 284.7 eV is characteristic of aliphatic C—C bonds, present within dendritic glycol structures. A contribution from the underneath NDs may also be considered, but expected intensity would be low [42,43].

TGA was employed to investigate the degree of surface modification of NDs. In Fig. 2f, presenting the results for **NDs-C** and **NDs-C-HPG** particles, the red lines represent the thermogravimetric (TG) curves, while the blue lines represent the first derivatives of the TG curves – DTG. As illustrated in Fig. 2f, the weight loss of acid-carboxylated nanodiamonds (**NDs-C**) was only 3.0 %, and the process starts at around 400 °C. The acid-carboxylated NDs modified with HPG (**NDs-C-HPG**) decomposed in a two-step process: first, between 220 °C and 450 °C, with a weight loss of 8 %, and second, between 450 °C and 900 °C, with a 2.2 % mass change. The initial step is associated with HPG decomposition. Under the reasonable assumption that no molecules or compounds other than HPG were conjugated to the surfaces of **NDs-C** particles during their modification via ROP of glycidol, the curves in Fig. 2f lead to a conclusion that HPG constitutes 8 % of the initial mass (≈5.9 mg) of **NDs-C-HPG** sample.

The thermal stability of plasma-oxygenated NDs (**NDs-O**) and plasma-oxygenated NDs modified with HPG (**NDs-O-HPG**) is illustrated in Fig. 2g. The weight loss of **NDs-O** is similar to that of **NDs-C** sample, being 3.3 %, and this process begins at around 400 °C. **NDs-O-HPG** particles, alike **NDs-C-HPG**, exhibit a two-step decomposition process. The first step occurs in the same temperature range as for **NDs-C-HPG**, with a mass change of 11.5 %, and the second step results in a mass change of 2 %. This leads to the same conclusion as in the case of **NDs-C-HPG** particles: HPG accounts for approximately 8 % of the initial mass of **NDs-O-HPG** sample.

3.2. Colloidal stability of HPG-modified NDs

Mean hydrodynamic diameters (d_H) and average zeta potentials of NDs saturated with oxygen-containing groups (**NDs-O**, **NDs-C**) or modified with HPG (**NDs-O-HPG**, **NDs-C-HPG**) are plotted against the initial pH values (2.00–12.00) of their corresponding aqueous dispersion media in Fig. 3a–d. Table 1 presents pH values of the supernatants obtained by removing NDs from the dispersion media through centrifugation. The colloidal properties of the oxygen-terminated particles (**NDs-O** and **NDs-C**) undergo similar changes with variations in pH (Fig. 3a,b). At mildly acidic values and in the whole alkaline region under observation (pH 4–12 for **NDs-C**, pH 5–12 for **NDs-O**), the particles exhibit zeta potentials below −40 mV (signifying good colloidal stability) [44] and stable values of d_H around ≈140 nm. In water-based solutions, –COOH groups present on the surfaces of **NDs-O** and **NDs-C** undergo dissociation, which results in negative values of the zeta potentials and a decrease of pH in the dispersion media [45]. This is evidenced in Table 1, which shows that introducing **NDs-O** and **NDs-C** particles to the aqueous solutions with initial pH from 8.00 to 10.00 has resulted in a neutralization of the liquids' alkalinity. Large numbers of hydrogen ions contained in highly acidic solutions (pH 2–3) counter-charge the negative surfaces of **NDs-O** and **NDs-C** [45], which causes the zeta potential values to rise above −26 mV, signaling incipient instability. Disrupted colloidal stability results in increasing d_H, which in the worst case (initial pH of the solution equal to 2.00) reaches 1205 nm for **NDs-O** and 1080 nm for **NDs-C** particles.

Compared to **NDs-O** and **NDs-C**, the particles modified with HPG exhibit visibly enhanced colloidal stability (Fig. 3c,d) in relation to pH. No aggregation of HPG-modified NDs was observed in the investigated pH range, and the mean hydrodynamic diameters of the particles showed stable values around ≈156 nm for **NDs-O-HPG** and ≈170 nm for **NDs-C-HPG**. The fact that the hydrodynamic diameters reported for **NDs-C-HPG** are 14 nm larger than for **NDs-O-HPG** may additionally confirm the more efficient surface modification of **NDs-C-HPG**. Zeta potentials of HPG-modified NDs have notably lower magnitudes than **NDs-O** and **NDs-C** due to lower accessibility of carboxyl groups to deprotonation, since large number of these groups served as surface sites for the attachment of HPG. At every investigated pH value, the zeta potentials of **NDs-O-HPG** are characterized by larger magnitudes than **NDs-C-HPG**, which results from unequal surface coverage of **NDs-O-HPG** and **NDs-C-HPG** particles with hyperbranched polyglycerol. FTIR spectra, SEM images, and hydrodynamic diameters reveal that HPG-modified nanodiamonds that had been subjected to plasma oxygenation (**NDs-O-HPG**) are covered with the polymer to a lesser extent than particles previously carboxylated in acids (**NDs-C-HPG**). Unreacted carboxyl groups deprotonate in aqueous solutions, inducing a negative surface charge. Since for **NDs-C-HPG** particles a larger percentage of the carboxyl groups underwent the chemical reaction to bind HPG, for **NDs-O-HPG** particles the magnitude of the (negative) zeta potential is higher.

At certain pH values (2–3 for **NDs-O-HPG**; 2–3 and 12 for **NDs-C-HPG**), the magnitudes of the zeta potentials are low enough to indicate substantial instability. The noteworthy inconsistency between selected values of the zeta potential (implying lack of colloidal stability) and mean hydrodynamic diameters (confirming very good colloidal stability) may be elucidated as an effect of surface modification with HPG. Yoshikawa et al. [46] revealed that colloidal stability of DNDs conjugated with HPG and suspended in water-based solutions results from strong but short-range steric repulsive potential barrier formed by polyglycerol, and not from the long-range but weak electrostatic repulsion between the electrical double layers, which under electric field set the particles in motion, creating a scattering signal detected during ELS measurements.

Fig. 3e,f presents intensity-based particle size distributions of **NDs-C** and **NDs-C-HPG** dispersed in 10 × concentrated PBS. Size distributions for **NDs-O** and **NDs-O-HPG** are presented in Fig. S4 in the Supplementary Information. Mean hydrodynamic diameters of the particles, as well as their 10th, 50th and 90th size percentiles – $d_i(10)$, $d_i(50)$ and $d_i(90)$, respectively – are provided in Table S2 in the Supplementary Information. NDs carboxylated in acids but not modified with HPG (**NDs-C**) are not resistant to high concentrations of salts present in the concentrated buffer solution, which makes them prone to instant aggregation upon dispersion. The extent of this aggregation is very large, as d_H of **NDs-C** is more than 10 times greater than d_H of the same particles dispersed in DMF (d_H = 146 nm; Fig. S5 in the Supplementary Information). In

MOST WIEDZY

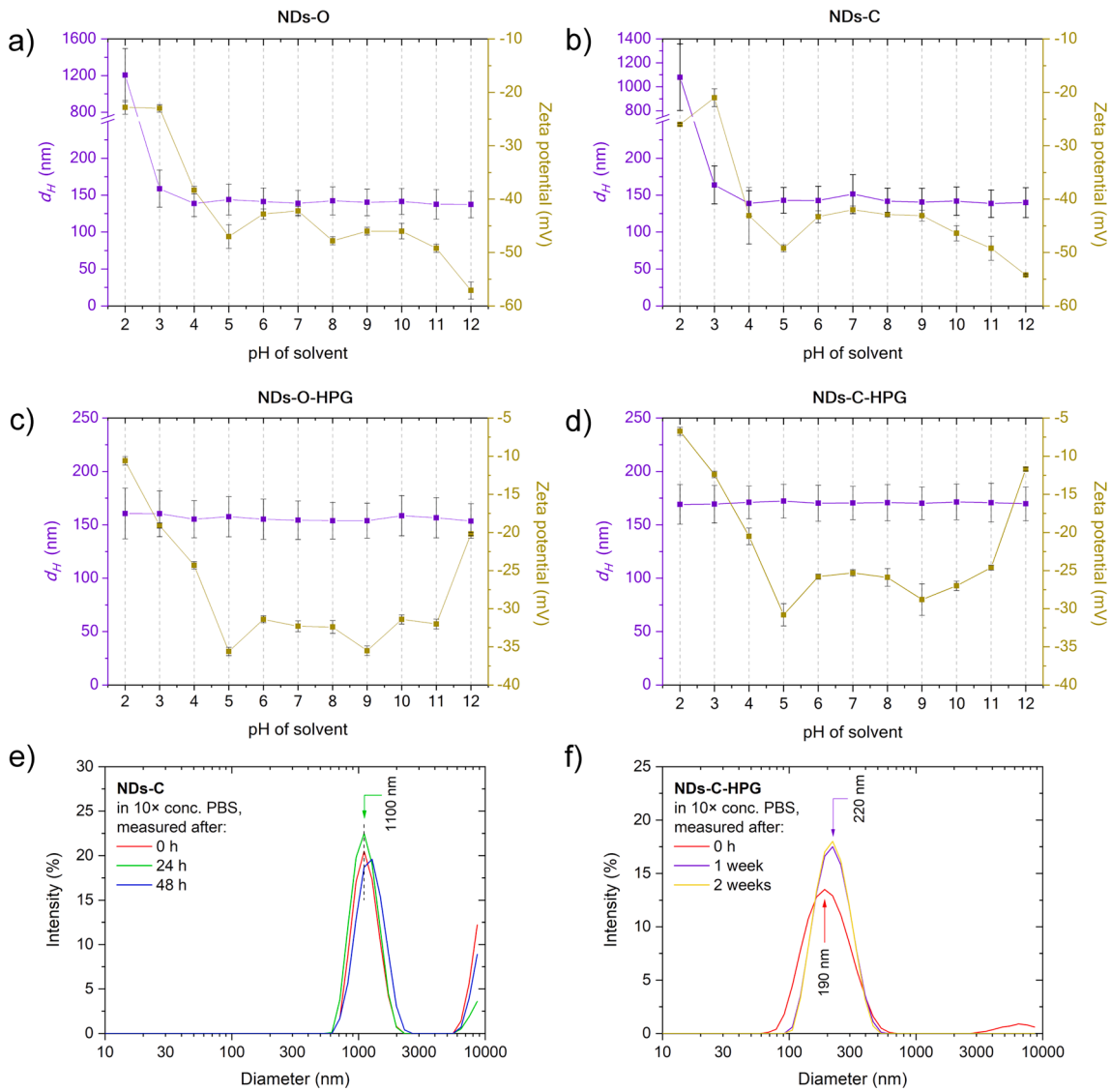

Fig. 3. a–d) Mean hydrodynamic diameters (d_H) and average zeta potentials of: a) plasma-oxygenated NDs (**NDs-O**); b) acid-carboxylated NDs (**NDs-C**); c) plasma-oxygenated NDs modified with HPG (**NDs-O-HPG**); d) acid-carboxylated NDs modified with HPG (**NDs-C-HPG**); the error bars represent standard errors of the mean for d_H values and standard deviations for zeta potential values; e) Intensity-weighed particle size distributions of **NDs-C** suspended in 10 × concentrated PBS, measured 0 h, 24 h, and 48 h after the dispersion; f) Intensity-weighed particle size distributions of **NDs-C-HPG** suspended in 10 × concentrated PBS, measured 0 h, 1 week, and 2 weeks after the dispersion.

addition to the fraction of the particles with diameters in the range of 700 nm–2 μm, the size distribution reveals very large aggregates, sizes of which start at ≈6.5 μm and extend to values beyond the detection limit (10 μm) of the analyzer used to perform the measurements [47].

Particle size distribution of **NDs-C-HPG** (Fig. 3f) reveals that colloidal stability of HPG-modified NDs is only marginally affected by the severe numbers of ions present in concentrated PBS. The dispersibility of **NDs-C-HPG** is largely preserved after 2 weeks, as the particles remain monodisperse with no large, micrometer-sized aggregates. While d_H of the particles is slightly higher than in pH-resolved measurements, the increase is not severe, and NDs with sizes not exceeding 200 nm are applicable in cellular uptake [9]. It should also be taken into consideration that mean hydrodynamic diameters determined in DLS measurements are larger than actual sizes of the particles due to the presence of electric double layers (which shrink in thickness with increasing salt concentration [48]) and solvated water molecules [49]. Particle size distributions of **NDs-O** and **NDs-O-HPG** dispersed in 10 × concentrated PBS (Fig. S4 in the Supplementary Information) additionally confirm the stabilizing effect of HPG. While **NDs-O** immediately undergo substantial aggregation, **NDs-O-HPG** particles remain well-dispersed for at least 2 weeks.

3.3. Performance of HPG-modified NDs in cell culture media

Fig. 4a,b presents intensity-based size distributions of **NDs-C** and **NDs-C-HPG** particles dispersed in diluted FBS and diluted DMEM, respectively. Mean hydrodynamic diameters (d_H) of the particles, as well as their 10th, 50th, and 90th size percentiles – $d_i(10)$, $d_i(50)$ and $d_i(90)$, respectively – are provided in Table S2 in the Supplementary Information. **NDs-C** suspended in DMEM, which contains both salt and proteins, undergo aggregation to an even greater extent than in concentrated PBS. The mean hydrodynamic diameter (d_H) of **NDs-C-DMEM**, equal to 1614 nm, confirms the loss of colloidal stability and signifies the upcoming flocculation of the particles. The aggregation of **NDs-C-FBS** is much less severe, which may arise from the dissimilar compositions of FBS and DMEM. Hemelaar et al [6] informed of a greater aggregation of NDs in DMEM compared to FBS and explained it with the principal role of NaCl, which is a component of DMEM and does not occur in FBS.

MOST WIEDZY

Table 1
Initial pH values of the dispersion media, and resulting pH values of nanodiamond suspensions.

Initial pH	Resulting pH			
	NDs-O	NDs-O-HPG	NDs-C	NDs-C-HPG
2.00	2.00	2.04	2.04	2.04
3.00	2.58	3.05	3.06	3.03
4.00	4.08	4.20	4.23	4.10
5.00	6.80	4.99	6.73	4.94
6.00	5.83	6.12	6.18	5.93
7.00	6.12	6.41	6.40	6.24
8.00	6.58	6.61	6.51	6.58
9.00	6.62	7.00	6.60	6.94
10.00	6.85	7.39	6.90	7.06
11.00	9.71	9.77	10.11	8.99
12.00	11.79	11.89	11.83	11.77

Fig. 4c displays **NDs-C** and **NDs-C-HPG** samples after the incubation in diluted FBS. As shown, the TG and DTG curves for **NDs-C-HPG-FBS** (Fig. 4c) and **NDs-C-HPG** (Fig. 2f) exhibit the same two-step decomposition process, with a total mass loss of approximately 9 %. Matching traces of TG curves for **NDs-C-HPG** and **NDs-C-HPG-FBS**, considering the difference in mass loss between the two samples to be of statistical nature, implies that proteins contained in FBS did not form the hard corona on the surfaces of HPG-modified NDs. In contrast, **NDs-C-FBS** particles (Fig. 4c) undergo a three-step decomposition process: the first between 140 °C and 500 °C, resulting in a mass loss of around 7 %. The DTG curve shape suggests an overlap of this process with the decomposition of different functional groups of FBS and decomposition of **NDs-C**. The second decomposition process, between 500 °C and 665 °C, is linked to further decomposition of **NDs-C**. The last decomposition step, from 665 °C to 900 °C, is associated with the decomposition of remaining functional groups of FBS, with a mass loss of 7.8 %.

Fig. 4d compares **NDs-C-DMEM** and **NDs-C-HPG-DMEM** samples. In

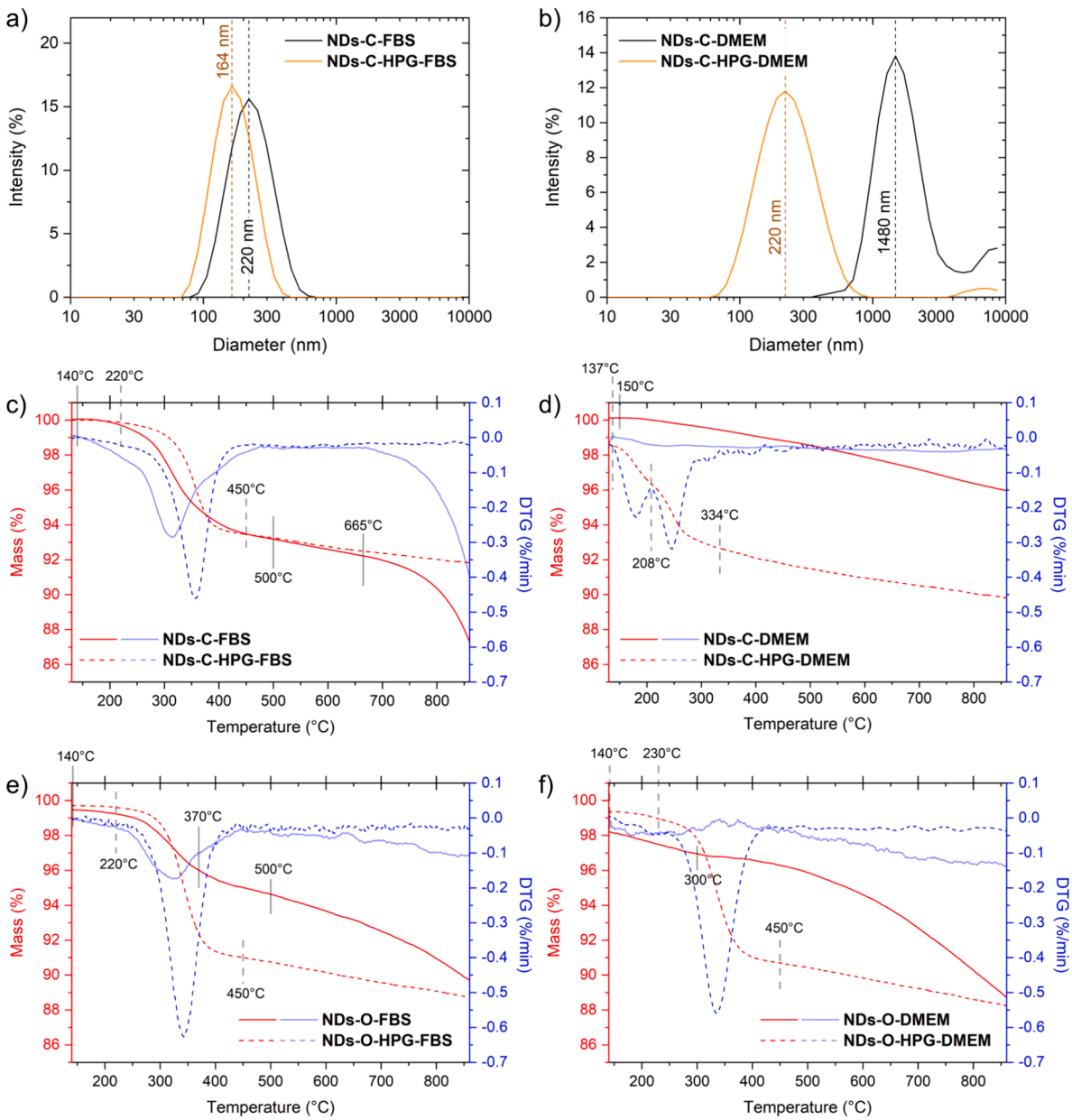

Fig. 4. a,b) Intensity-weighed particle size distributions of: a) **NDs-C** and **NDs-C-HPG** suspended in FBS:water mixture; b) **NDs-C** and **NDs-C-HPG** suspended in DMEM:water mixture; c-f) thermogravimetric (TG) and derivative thermogravimetric (DTG) curves of: c) **NDs-C-FBS** and **NDs-C-HPG-FBS**; d) **NDs-C-DMEM** and **NDs-C-HPG-DMEM**; e) **NDs-O-FBS** and **NDs-O-HPG-FBS**; f) **NDs-O-DMEM** and **NDs-O-HPG-DMEM.**

MOST WIEDZY

the TG curve of **NDs-C-DMEM**, a continuous one-step decomposition process is observed, with a total mass loss of 4.4 %. The higher percentage of mass loss compared to **NDs-C** suggests that selected components of DMEM could adsorb on the sample surface, especially as the decomposition begins at around 150 °C, a much lower temperature than for the **NDs-C** sample. A notable difference for the **NDs-C-HPG-DMEM** sample is observed after a 1-hour isotherm at 137 °C, with a 1.5 % mass weight loss. The initial decomposition step occurs between 137 °C and 208 °C, suggesting that this decomposition starts during the isothermal sample heating. The weight loss during this process equals 2.2 %. The subsequent decomposition step takes place between 208 °C and 334 °C, resulting in a mass loss of 3.7 %, and is connected with the first decomposition process. Based on the shape of the DTG curve and the temperature range, it can be concluded that these processes are linked to the decomposition of DMEM adsorbed on the sample.

Thermal decomposition of **NDs-O-FBS** and **NDs-O-HPG-FBS** is illustrated by curves in Fig. 4e. **NDs-O-FBS** particles undergo decomposition in similar temperature ranges as **NDs-C-FBS**. The first step (from 140 °C to 370 °C) and the second one (up to 500 °C) overlap each other and are accompanied by a 4.9 % mass loss. Next, the continuous decomposition process up to 900 °C results in a 5.9 % mass loss. The total mass loss in **NDs-O-FBS** sample is substantially larger than in the corresponding sample unincubated in FBS (**NDs-O**, Fig. 2g), which suggest formation of hard protein corona on the surfaces of **NDs-O-FBS** particles. **NDs-O-HPG-FBS** (Fig. 4e) particles exhibit identical thermal stability as **NDs-O-HPG** sample (Fig. 2g). The sample is characterized by a two-step decomposition process, with the first step (from 220 °C up to 450 °C) resulting in a 9 % mass loss, and the second step (between 450 °C and 900 °C) resulting in a 2.5 % mass loss, which is statistically similar to **NDs-O-HPG**. No additional mass loss was observed for **NDs-O-HPG-FBS** in relation to **NDs-O-HPG**, which leads to a conclusion that HPG grafted on the surfaces of the plasma-oxygenated NDs successfully inhibits the formation of a hard protein corona.

Fig. 4f compares TG and DTG curves of **NDs-O-DMEM** and **NDs-O-HPG-DMEM** samples. **NDs-O-DMEM** particles show a similar behavior to **NDs-C-DMEM** (Fig. 4d) particles. The decomposition process also starts during the 1-hour isotherm and is characterized by a mass change of 1.8 %. For the **NDs-O-DMEM** sample, a two-step decomposition process occurs: the first step up to 300 °C with a mass change of 1.3 %, and the second step up to 900 °C with a 9.4 % mass loss. The total mass loss for the two-step decomposition of the **NDs-O-DMEM** particles is 10.7 %, which is much higher than that for the **NDs-C-DMEM** sample. This may suggest that plasma-oxygenated NDs can adsorb significantly more DMEM compounds than acid-carboxylated NDs. The stability of DMEM on the **NDs-O-HPG** surface (Fig. 4f) is characterized by similar decomposition steps as observed for **NDs-C-HPG-DMEM** (Fig. 4d). The first step occurs between 140 °C and 230 °C with a 0.5 % mass loss, the second step occurs between 230 °C and 450 °C with an 8.3 % mass loss, and the final step, up to 900 °C, is characterized by a 2.7 % mass loss.

3.4. Fluorescence of HPG-modified NDs

Fluorescence spectra of **NDs-C** dispersed in a few selected pH-diverse solutions are shown in Fig. 5a. These spectra were averaged from 3 successive measurements and normalized to the maximum value of the photon counts recorded for non-modified NDs, that is, for **NDs-O** at a pH of 11. Each spectrum of **NDs-O** and **NDs-C** consist of a similar-looking, wide band reaching its maximum at ≈ 593 nm and lacking local characteristic features except for a weak peak at 657 nm, which comes from the dispersion media and is a consequence of an imperfect background subtraction. The fluorescence spectrum of an aqueous solution without NDs (Fig. 5a, inset) confirms the origins of this peak. The spectra registered for **NDs-O** and **NDs-C** are typical for the intrinsic fluorescence of diamonds containing low numbers of color centers. The bands with similar structures were reported for laser-synthesized NDs [50] and DNDs [51]. The position of the global maximum of the band is excitation wavelength-dependent, i.e. it is claimed to move towards longer wavelengths as the excitation wavelength increases [51,52].

The fluorescence spectra of **NDs-O** and **NDs-C** particles were integrated over the wavelength range of 550–800 nm, and the total numbers of photon counts (the areas under the curves) were plotted versus the original pH values of the corresponding dispersion media (Fig. 5b) to provide a clear understanding of how pH affects the total emission efficiency of non-modified NDs. Once more, the calculated data were normalized to the maximum value found in the series. Fig. 5b shows that both **NDs-O** and **NDs-C** emit most intensively in a highly alkaline environment (pH of solvent equal to 11), and the total numbers of photon counts decrease nearly monotonically as the pH of the surroundings drops, which is in line with earlier findings [51]. For both **NDs-O** and **NDs-C** particles, the lowest emission efficiency was observed upon dispersion in the most acidic aqueous solution (pH of 2). In contrast with Reineck et al. [51], the reduction in the number of photon counts in this study may partly result from the worsening colloidal stability of non-modified NDs in acidic conditions. The formation of aggregates reduces the effective surface area exposed to excitation upon illumination, and sedimentation results in larger variations in the number of particles in the laser light path.

Fig. 5c presents exemplary fluorescence spectra of **NDs-C-HPG** particles dispersed in aqueous solutions with varied pH. Like for non-modified NDs, these spectra were averaged from 3 measurements and normalized to the maximum number of photon counts recorded in the series, which in this case was the signal emitted by **NDs-C-HPG** at pH of 10. HPG does not introduce additional characteristic peaks to the spectra and does not obscure the collection of the fluorescence, which makes it applicable in optical sensing purposes. The spectra of **NDs-C-HPG** (Fig. 5c) are notably less noisy than the signals collected from **NDs-C** (Fig. 5a), which may be explained by a larger difference in refractive indices between pristine diamond (2.42) and water (1.33) than between polyglycerol (1.47) [53] and water (1.33). Deprotonation of carboxyl (–COOH) groups significantly increases the negative charge on the oxygen atoms. This heightens the overall negative surface charge of NDs, reducing their tendency to form aggregates. This in turn allows them to attract and bind a dense layer of water molecules, forming a hydration shell encapsulating each particle. The surrounding water molecules quench (suppress) the emission of fluorescence from NDs.

The total photon counts registered for **NDs-C-HPG** and **NDs-O-HPG**, calculated through the integration of the fluorescence spectra over 550–800 nm range, are plotted against the initial pH values of the aqueous dispersion media in Fig. 5d. The emission efficiency of **NDs-C-HPG** is substantially higher than **NDs-O-HPG**. **NDs-C-HPG** particles take advantage of the high affinity of densely packed carboxyl groups towards HPG formation process, significantly increasing the modification of NDs. In the FTIR spectrum of **NDs-C-HPG** (Fig. 2a), the well-formed absorption bands of NDs are obscured by HPG bands (2800–3000 cm^{-1}), which are produced by the overlapping of C—H stretching of polyglycerol tails [10], indicating a high level of conjugation with –COOH groups. This is also noticed as enhanced fluorescence brightness compared to **NDs-O-HPG** (Fig. 5d). Carboxyl groups saturated with HPG significantly enhance the homogeneity of NDs and improve the efficiency of modifying their surfaces, potentially being the reason for the increase in brightness jointly with carbon-dot-like fluorescence [54]. Improving the amount of carboxylic acid on the surfaces of nanoparticles increases the efficiency of subsequent conjugation reactions, as carboxylic acids are linked to the surfaces of nanoparticles by several atom spacers, which may reduce steric constraints and enhance the efficiency of subsequent surface chemistry [55].

Significantly, for both **NDs-C-HPG** and **NDs-O-HPG**, the photon counts remain stable and do not decrease even when the pH of the dispersion media becomes highly acidic, revealing the high stability of the emitted fluorescence signal across a wide pH range. The drop in fluorescence typically observed at pH values below 6 does not occur for these nanodiamond conjugates. In general, the source of fluorescence in

MOST WIEDZY

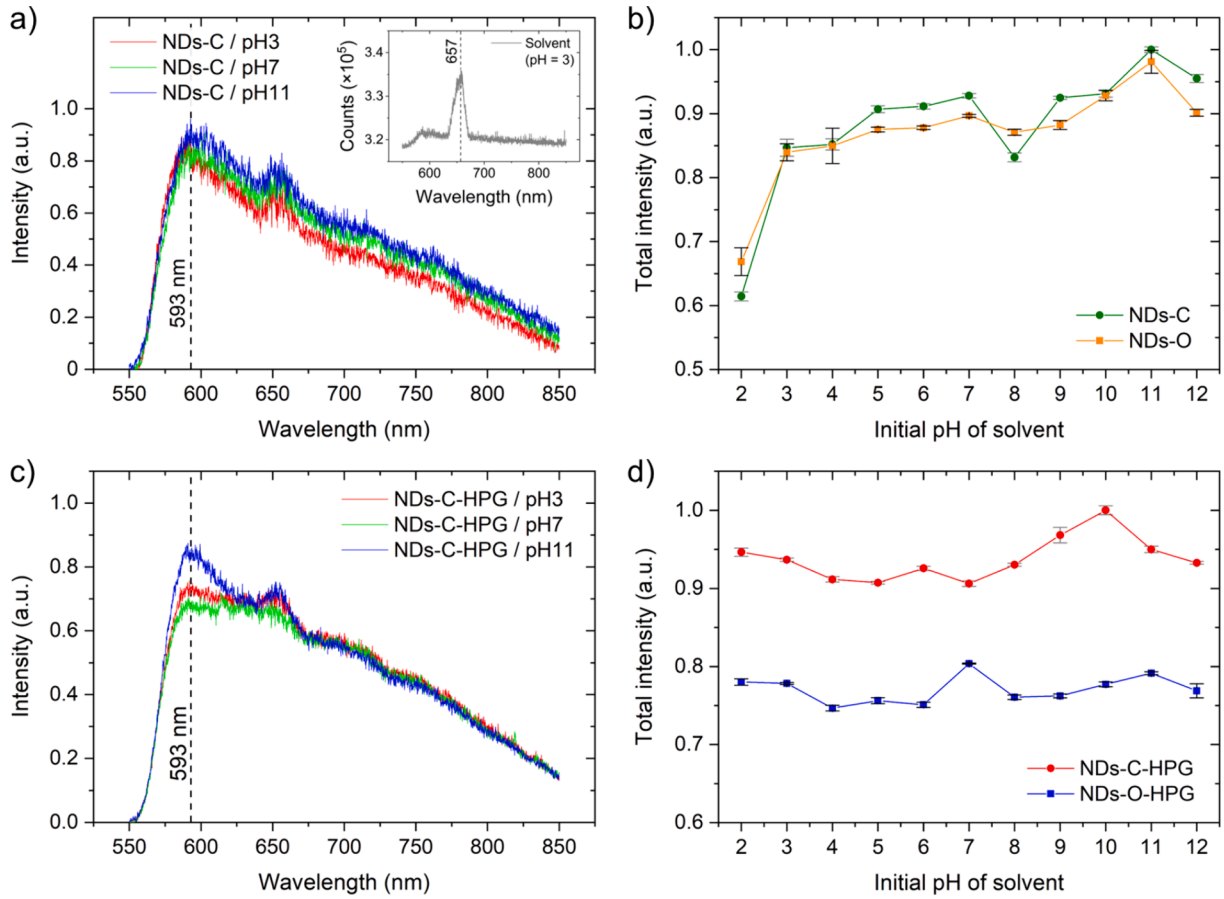

Fig. 5. Fluorescence spectra of a) **NDs-C** and c) **NDs-C-HPG** suspended in media with the initial pH of 3 or 7 or 11; Integrated fluorescence of b) **NDs-O**, **NDs-C** and d) **NDs-O-HPG**, **NDs-C-HPG** vs. the initial pH of their dispersion media; the inset to Fig. 5a presents unprocessed fluorescence spectrum of the aqueous solvent with a pH of 3.00.

HPHT nanodiamonds is related to the presence of various defects in the diamond structure, such as N3, H3, H4, carbon-dot-like or NV centers. Their quantum efficiencies are sensitive to different types of surface functionalization as well as environmental conditions, which tailor their emission. Here, the fluorescence spectra of **NDs-C-HPG** and **NDs-O-HPG,** excited by 532 nm, are likely associated with H3– and H4-related emissions, showing a broad band from ≈550 to 650 nm, previously recorded at 530–580 nm under blue excitation of HPHT-treated samples [56]. The bands are shifted to higher wavelengths and have a wider tail toward the red side [57]. It should be noted that this band may also be partially superposed by an N3-originated band, since most HPHT diamonds reveal characteristic asymmetric broad emission band associated with N3 centers located at ≈560 nm [58].

The fluorescence results underline a profound influence of surface chemistry of nanomaterials on their performance within biologically relevant conditions. Preserving strong fluorescence across a wide range of pH levels, including highly acidic settings, proves the essential function of HPG-based modifications in protecting against environmental variables. In biological sensing and imaging, the reliability and uniformity of optical signals are crucial for the precise tracking of nanomaterials or the processes they are involved in, e.g., drug delivery [59] or thermal treatments [20], enabling accurate data analysis and, ultimately, accurate diagnostics. The results obtained in this study reveal that surface modification of NDs with HPG preserves their inherent fluorescence, while broadening their utility in intricate biological environments. First, this approach allows for fixing selective linkers or receptors to the HPG-modified ND surfaces, as shown in [14,16–18,60]. Such modifications enable the creation of materials specifically designed to be sensitive to targeted interactions, while minimizing unwanted binding with other biomolecules. What is particularly noteworthy is that modification with HPG offers additional benefits to the molecules beyond promoting stable attachment of compounds. For instance, it can significantly enhance the water solubility of substances, such as drugs, increase the capacity for drug/substance loading, and even boost the effectiveness of photodynamic therapy treatments, as shown in the work of Xiang et al. [61]. Moreover, in the context of proteins or drugs frequently attached to HPG as receptors, linkers, or targeting agents, research such as the one conducted by Tully et al. [62] has shown that HPG can significantly extend their half-life by safeguarding the molecules against enzymatic degradation, or immune detection. The exceptional biocompatibility of HPG, as confirmed by numerous studies and its multifaceted features, positions it as a promising candidate for future research and applications in nanomedicine [62,63]. The integration of HPG with fluorescent NDs creates a powerful synergy, paving the way for the development of adaptable, stable, and biocompatible nanomaterials. These advanced materials are ready to meet various biomedical needs and environmental monitoring challenges, showcasing the potential to revolutionize diagnostics, therapeutic delivery, and biosensing technologies. Future studies may further explore the mechanisms underlying the interaction between HPG-modified NDs – including NDs embedded with color centers, particularly nitrogen-vacancy centers – and biological systems, aiming to enhance their functionality, optimize their design for targeted applications, and address any challenges in their practical deployment.

MOST WIEDZY

3.5. Molecular dynamics simulations of the interactions between non-modified and HPG-modified NDs

To provide a molecular-level explanation of the improved colloidal stability of HPG-modified NDs, a minimal atomistic model, featuring a single HPG molecule (Fig. S2 in the Supplementary Information) attached to the (1 0 0) surface of a periodic 3.5 × 3.5 nm nanodiamond slab, was constructed (see Chapter 2.7). While recognizing the potential variations in the grafting density and size of HPG molecules in real-world scenarios, the model captures the altered chemical nature of the surface of the nanoparticle, and at the same time is compact enough to allow for direct study of the interaction between the surfaces.

In order to limit the space of possible HPG models, the simulation study of differently branched HPG grafted on the mentioned diamond surface was performed. A series of differently branched HPG models was created (Fig. S6 in the Supplementary information). This simulation assumed that the HPG structure can grow only symmetrically; thus, each branch has an equal length. As a level of branching, the number of glycidol monomers in the branch is taken; that is, HPG level 3 has 3 glycidol monomers in each branch. The created structures were subjected to 10-ps MD simulation using the Slater–Koster tight-binding model (DFTB) [64]. The "mio-1–1" [64–66] Hamiltonian parametrization was selected [66] as published in dftb.org databases. The application of DFTB method allows for simulation without constraining the structure topology; that is, the bond-breaking/creation process was possible.

The approach was applied for HPG with branching levels from 2 to 5 (Fig. 6a), structures of which were generated using in-house development scripts, and preoptimized using UFF force field [67]. For branching levels from 2 to 4, the alternative grafting pattern was tested. This pattern assumes that the glycidol monomers from the top level of branching are placed directly on the surface, simulating that instead of extending existing HPG structure, new chains start to form (Fig. S6 in the Supplementary information). For each case, the cohesion (atomization) energy was calculated. It was found that each structure does not break apart during the MD simulation, proving that HPG is stable on (1 0 0) diamond carboxylated surface, which is supported by significantly negative atomization energy for each case (Fig. 6a). The difference in cohesion energies between pure HPG grafting and HPG surrounded by glycidol was not larger than 10^{-4} eV, thus it was insignificant. The largest stable HPG structure was therefore prepared for the next, longer MD simulation with the application of force field with fixed bond topology in order to study the structure conformation.

To characterize the conformational properties and arrangement of HPG molecules on the (1 0 0) and (1 1 1) surfaces of ND, the models were subjected to 500 ns of MD simulation in an explicit solvent containing 1.5 M NaCl, which corresponds to 10 × concentrated PBS (Video S1 in the Supplementary Information). The analysis of density profiles derived from these simulations (Fig. 6b and Fig. S7) unveils a very similarly structured HPG matrix at both ND facets. Specifically, the highest density peak in the HPG profile, occurring at 0.4 nm from the surface, arises from favorable van der Waals interactions between HPG and the ND surfaces. Accumulation of polyglycerol chains at the surface induces long-range ordering within the HPG matrix, with the successive density

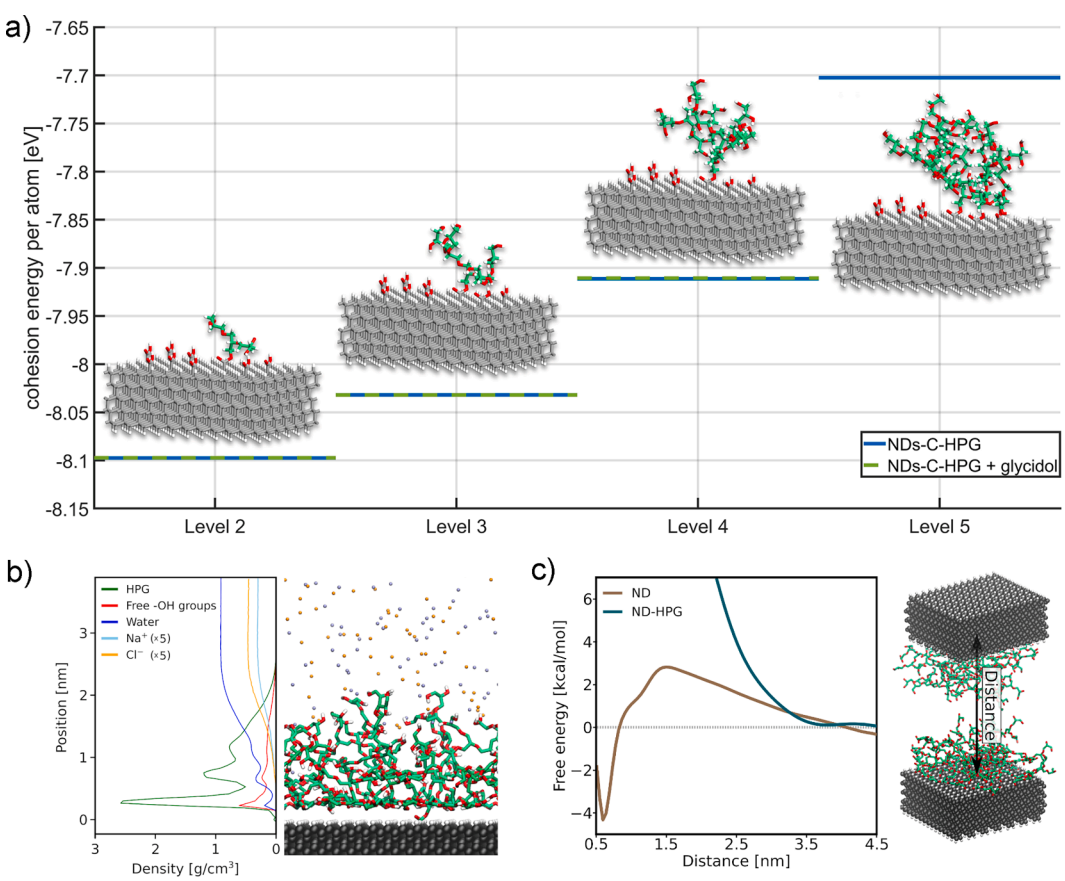

Fig. 6. a) The series of slab models used in the DFTB MD simulation, HPG without alongside glycidol and resulting cohesion energies of the structures; b) density profiles describing the structure of the HPG film as a function of the distance from the (1 0 0) ND surface, derived from MD simulations (for the (1 1 1) ND surface results, please see Fig. S7). Ion densities were scaled by a factor of 5 for clarity. The variations in density are visually depicted by the molecular representation on the right. For equivalent data acquired at a double grafting density, refer to Fig. S8 in the Supplementary Information; c) Free energy profile for the association between two parallel ND slabs through (1 0 0) surfaces in the absence (ND) and presence (ND-HPG) of HPG modifications. The separation distance between the surfaces was used as the reaction coordinate.

MOST WIEDZY

peaks gradually decreasing in height. This layered structure is even more pronounced for the ND-HPG system with doubled grafting density resulting in a 1.5-times thicker HPG film (Fig. S8 in the Supplementary Information).

Fig. 6b, along with Fig. S7 and Fig. S8 in the Supplementary Information, also reveals that the free hydroxyl groups are distributed relatively evenly across the HPG film, and the hydration level of HPG molecules varies significantly with grafting density, being lower in the doubled density case. Notably, monovalent ions are largely excluded from the ND vicinity by HPG, even at a concentration as high as 1.5 M. In the doubled density case, however, a certain degree of ion binding is observed within the second HPG layer at 0.65 nm from the ND surface with no discernible selectivity between cations and anions.

To examine the effect of the surface modification with HPG on interparticle interaction, the free energy profile was calculated for the association between two parallel ND slabs, utilizing the separation distance between the surfaces as the reaction coordinate (see Fig. 6c, left and Experimental for details). For comparison, this was done separately either for free ND surfaces or for surfaces modified with HPG molecules. Since the structure and dynamics of HPG is nearly the same on the (1 0 0) and (1 1 1) surfaces, the free energy calculations were performed only for the former. As can be seen in Fig. 6c, in the absence of HPG, the profile shows a well-pronounced free energy minimum of −4.5 kcal/mol at 0.6 nm, corresponding to direct contact between the surfaces with a very low activation barrier for association (3 kcal/mol at 1.5 nm). Consistently with the particle size measurements, this result indicates that electrically neutral ND surfaces, as found in acidic pH or high salt concentration conditions, tend to aggregate due to hydrophobic interactions, leading to instability of the particles. In contrast, when the surfaces are modified with HPG, the profile undergoes a dramatic change. The bound state minimum disappears entirely, replaced by a steep free energy barrier that prevents the surfaces to approach each other closer than 2.5 nm. Given that the thickness of the HPG film in the model is approximately 1.5 nm (Fig. 6b), it is evident that this strong repulsion arises from overlapping of the polyglycerol films from opposite ND surfaces. This result indicates that enhanced colloidal stability of HPG-modified NDs arises from short-range steric forces between overlapping polyglycerol coatings, corroborating earlier findings [46].

4. Conclusions

In this study, commercially available NDs (140 nm in size) produced by HPHT process were conjugated with HPG using a simple reaction of anionic ROP of glycidol. Prior to the modification, the NDs were oxygenated in plasma or carboxylated in acids to saturate their surfaces with oxygen-containing groups. HPG, whose presence on the surfaces of NDs was confirmed using FTIR and XPS, does not hinder the optical addressability of the particles and makes it possible to equalize levels of the intrinsic fluorescence of diamond relative to pH of dispersion media. At the same time, HPG provides the NDs with excellent colloidal stability in highly acidic aqueous solutions, concentrated PBS and cell culture media, which was confirmed using DLS. MD calculations support these findings, revealing that HPG induces substantial changes to free energy profiles for modified NDs interacting with each other, and generates short-range steric repulsive forces which keep the particles well-dispersed even in severely ionic environments. TGA showed that HPG successfully inhibits the nonspecific adsorption of proteins to the surfaces of NDs, preventing the formation of hard protein corona. In conclusion, the modification demonstrated in this work makes it possible to engineer NDs that are both immune to aggregation in a variety of environments, while at the same time being easily addressed for optical detection.

The surface modification demonstrated in this study is possible to be performed on NDs implanted with color centers (nitrogen-vacancy centers in particular) to engineer stable platforms for optical detection inside cellular environments. It is worth pointing out that NDs produced by HPHT method, the type that was used in this study, are most commonly chosen for implantation with color centers. The enhanced colloidal stability granted by HPG could make it possible to exploit the favorable sensing capabilities of color centers within physiological environments, expanding the potential for optical measurements of physical quantities. In the future, the modification with HPG may also be expanded by attaching selective linkers or receptors to HPG immobilized on the surfaces of NDs to engineer composite platforms that are sensitive to selected interactions while resistant to adhesion of any other biomolecules.

Declaration of generative AI in scientific writing

During the preparation of this work, the author(s) used CLAUDE to check grammar. After using this tool, the authors reviewed and edited the content as needed and took full responsibility for the content of the publication.

CRediT authorship contribution statement

Maciej J. Głowacki: Writing – review & editing, Writing – original draft, Validation, Methodology, Investigation, Formal analysis, Data curation, Conceptualization. **Paweł Niedziałkowski:** Writing – original draft, Visualization, Validation, Resources, Methodology, Investigation, Conceptualization. **Jacek Ryl:** Writing – original draft, Visualization, Methodology, Investigation, Formal analysis, Data curation. **Marta Prześniak-Welenc:** Writing – original draft, Visualization, Investigation. **Mirosław Sawczak:** Writing – original draft, Investigation. **Klaudia Prusik:** Investigation. **Mateusz Ficek:** Investigation. **Monika Janik:** Writing – original draft, Investigation, Conceptualization. **Krzysztof Pyrchla:** Writing – original draft, Visualization, Investigation, Formal analysis. **Michał Olewniczak:** Writing – original draft, Visualization, Investigation, Formal analysis. **Krzysztof Bojarski:** Writing – original draft, Visualization, Investigation, Formal analysis. **Jacek Czub:** Writing – original draft, Visualization, Methodology, Investigation, Formal analysis, Data curation. **Robert Bogdanowicz:** Writing – review & editing, Writing – original draft, Validation, Supervision, Resources, Project administration, Methodology, Funding acquisition, Conceptualization.

Declaration of competing interest

The authors declare that they have no known competing financial interests or personal relationships that could have appeared to influence the work reported in this paper.

Data availability

Data will be made available on request.

Acknowledgements

This research was carried out within the TEAM-NET program of the Foundation for Polish Science, co-financed by the European Union under the European Regional Development Fund (project no. POIR.04.04.00-00-1644/18). We gratefully acknowledge Polish high-performance computing infrastructure PLGrid (HPC Centers: ACK Cyfronet AGH, CI TASK) for providing computer facilities and support within computational grant no. PLG/2023/016164.

Appendix A. Supplementary data

Supplementary data to this article can be found online at https://doi.org/10.1016/j.jcis.2024.06.225.

MOST WIEDZY

References

[1] L.P. McGuinness, Y. Yan, A. Stacey, D.A. Simpson, L.T. Hall, D. Maclaurin, S. Prawer, P. Mulvaney, J. Wrachtrup, F. Caruso, R.E. Scholten, L.C.L. Hollenberg, Quantum measurement and orientation tracking of fluorescent nanodiamonds inside living cells, Nat. Nanotech. 6 (2011) 358–363, https://doi.org/10.1038/nnano.2011.64.

[2] B. Chang, H. Lin, L. Su, W. Lin, R. Lin, Y. Tzeng, R.T. Lee, Y.C. Lee, A.L. Yu, H. Chang, Highly fluorescent nanodiamonds protein-functionalized for cell labeling and targeting, Adv. Funct. Mater. 23 (2013) 5737–5745, https://doi.org/10.1002/adfm.201301075.

[3] K. Solarska-Ściuk, A. Gajewska, S. Glińska, M. Studzian, S. Michlewska, Ł. Balcerzak, J. Skolimowski, B. Kolago, G. Bartosz, Intracellular transport of nanodiamond particles in human endothelial and epithelial cells, Chem. Biol. Interact. 219 (2014) 90–100, https://doi.org/10.1016/j.cbi.2014.05.013.

[4] H. An, Z. Yin, C. Mitchell, A. Semnani, A.R. Hajrasouliha, M. Hosseini, Nanodiamond ensemble-based temperature measurement in living cells and its limitations, Meas. Sci. Technol. 32 (2021) 015701, https://doi.org/10.1088/1361-6501/abace7.

[5] H.-C. Chang, W.-W.-W. Hsiao, M.-C. Su, Fluorescent Nanodiamonds, Wiley, Hoboken, NJ, USA Chichester, West Sussex, UK, 2019.

[6] S.R. Hemelaar, A. Nagl, F. Bigot, M.M. Rodríguez-García, M.P. De Vries, M. Chipaux, R. Schirhagl, The interaction of fluorescent nanodiamond probes with cellular media, Microchim. Acta 184 (2017) 1001–1009, https://doi.org/10.1007/s00604-017-2086-6.

[7] T. Takimoto, T. Chano, S. Shimizu, H. Okabe, M. Ito, M. Morita, T. Kimura, T. Inubushi, N. Komatsu, Preparation of fluorescent diamond nanoparticles stably dispersed under a physiological environment through multistep organic transformations, Chem. Mater. 22 (2010) 3462–3471, https://doi.org/10.1021/cm100566v.

[8] Y.V. Kulvelis, A.V. Shvidchenko, A.E. Aleksenskii, E.B. Yudina, V.T. Lebedev, M. S. Shestakov, A.T. Dideikin, L.O. Khozyaeva, A.I. Kuklin, Gy. Török, M.I. Rulev, A. Ya. Vul, Stabilization of detonation nanodiamonds hydrosol in physiological media with poly(vinylpyrrolidone), Diam. Relat. Mater. 87 (2018) 78–89, https://doi.org/10.1016/j.diamond.2018.05.012.

[9] V. Merz, J. Lenhart, Y. Vonhausen, M.E. Ortiz-Soto, J. Seibel, A. Krueger, Zwitterion-functionalized detonation nanodiamond with superior protein repulsion and colloidal stability in physiological media, Small 15 (2019) 1901551, https://doi.org/10.1002/smll.201901551.

[10] S. Wang, Y. Zhou, S. Yang, B. Ding, Growing hyperbranched polyglycerols on magnetic nanoparticles to resist nonspecific adsorption of proteins, Colloids Surf. B Biointerfaces 67 (2008) 122–126, https://doi.org/10.1016/j.colsurfb.2008.08.009.

[11] D. Wilms, S.-E. Stiriba, H. Frey, hyperbranched polyglycerols: from the controlled synthesis of biocompatible polyether polyols to multipurpose applications, Acc. Chem. Res. 43 (2010) 129–141, https://doi.org/10.1021/ar900158p.

[12] Z. Rafiee, S. Omidi, Modification of carbon-based nanomaterials by polyglycerol: recent advances and applications, RSC Adv. 12 (2022) 181–192, https://doi.org/10.1039/D1RA07554C.

[13] L. Zhao, T. Takimoto, M. Ito, N. Kitagawa, T. Kimura, N. Komatsu, Chromatographic separation of highly soluble diamond nanoparticles prepared by polyglycerol grafting, Angew Chem Int Ed 50 (2011) 1388–1392, https://doi.org/10.1002/anie.201006310.

[14] J.-P. Boudou, M.-O. David, V. Joshi, H. Eidi, P.A. Curmi, Hyperbranched polyglycerol modified fluorescent nanodiamond for biomedical research, Diam. Relat. Mater. 38 (2013) 131–138, https://doi.org/10.1016/j.diamond.2013.06.019.

[15] M.H.M. Oudshoorn, R. Rissmann, J.A. Bouwstra, W.E. Hennink, Synthesis and characterization of hyperbranched polyglycerol hydrogels, Biomaterials 27 (2006) 5471–5479, https://doi.org/10.1016/j.biomaterials.2006.06.030.

[16] L. Zhao, Y. Nakae, H. Qin, T. Ito, T. Kimura, H. Kojima, L. Chan, N. Komatsu, Polyglycerol-functionalized nanodiamond as a platform for gene delivery: Derivatization, characterization, and hybridization with DNA, Beilstein J. Org. Chem. 10 (2014) 707–713, https://doi.org/10.3762/bjoc.10.64.

[17] S. Sotoma, R. Igarashi, J. Iimura, Y. Kumiya, H. Tochio, Y. Harada, M. Shirakawa, Suppression of nonspecific protein-nanodiamond adsorption enabling specific targeting of nanodiamonds to biomolecules of interest, Chem. Lett. 44 (2015) 354–356, https://doi.org/10.1246/cl.141036.

[18] H. Huang, M. Liu, R. Jiang, J. Chen, L. Mao, Y. Wen, J. Tian, N. Zhou, X. Zhang, Y. Wei, Facile modification of nanodiamonds with hyperbranched polymers based on supramolecular chemistry and their potential for drug delivery, J. Colloid Interface Sci. 513 (2018) 198–204, https://doi.org/10.1016/j.jcis.2017.11.009.

[19] D. Terada, S. Sotoma, Y. Harada, R. Igarashi, M. Shirakawa, One-pot synthesis of highly dispersible fluorescent nanodiamonds for bioconjugation, Bioconjugate Chem. 29 (2018) 2786–2792, https://doi.org/10.1021/acs.bioconjchem.8b00412.

[20] D. Maziukiewicz, R. Mrówczyński, S. Jurga, B.F. Grześkowiak, Laser synthesized nanodiamonds with hyper-branched polyglycerol and polydopamine for combined imaging and photothermal treatment, Diam. Relat. Mater. 128 (2022) 109308, https://doi.org/10.1016/j.diamond.2022.109308.

[21] P.-H. Chung, E. Perevedentseva, J.-S. Tu, C.C. Chang, C.-L. Cheng, Spectroscopic study of bio-functionalized nanodiamonds, Diam. Relat. Mater. 15 (2006) 622–625, https://doi.org/10.1016/j.diamond.2005.11.019.

[22] Y. Li, X. Zhou, Transferrin-coupled fluorescence nanodiamonds as targeting intracellular transporters: An investigation of the uptake mechanism, Diam. Relat. Mater. 19 (2010) 1163–1167, https://doi.org/10.1016/j.diamond.2010.05.003.

[23] M. Khan, W.T.S. Huck, Hyperbranched Polyglycidol on Si/SiO $_2$ Surfaces via Surface-Initiated Polymerization, Macromolecules 36 (2003) 5088–5093, https://doi.org/10.1021/ma0340762.

[24] K. Kvakova, M. Ondra, J. Schimer, M. Petrik, Z. Novy, H. Raabova, M. Hajduch, P. Cigler, Visualization of sentinel lymph nodes with mannosylated fluorescent nanodiamonds, Adv. Funct. Mater. 32 (2022) 2109960, https://doi.org/10.1002/adfm.202109960.

[25] E.R. Wilson, L.M. Parker, A. Orth, N. Nunn, M. Torelli, O. Shenderova, B.C. Gibson, P. Reineck, The effect of particle size on nanodiamond fluorescence and colloidal properties in biological media, Nanotechnology 30 (2019) 385704, https://doi.org/10.1088/1361-6528/ab283d.

[26] N. Raval, R. Maheshwari, D. Kalyane, S.R. Youngren-Ortiz, M.B. Chougule, R.K. Tekade, Importance of Physicochemical Characterization of Nanoparticles in Pharmaceutical Product Development, in: Basic Fundamentals of Drug Delivery, Elsevier, 2019: pp. 369–400. doi: 10.1016/B978-0-12-817909-3.00010-8.

[27] M.J. Abraham, T. Murtola, R. Schulz, S. Páll, J.C. Smith, B. Hess, E. Lindahl, GROMACS: High performance molecular simulations through multi-level parallelism from laptops to supercomputers, SoftwareX 1–2 (2015) 19–25, https://doi.org/10.1016/j.softx.2015.06.001.

[28] K. Vanommeslaeghe, A.D. MacKerell, Automation of the CHARMM General Force Field (CGenFF) I: Bond Perception and Atom Typing, J. Chem. Inf. Model. 52 (2012) 3144–3154, https://doi.org/10.1021/ci300363c.

[29] M. Parrinello, A. Rahman, Polymorphic transitions in single crystals: A new molecular dynamics method, J. Appl. Phys. 52 (1981) 7182–7190, https://doi.org/10.1063/1.328693.

[30] G. Bussi, D. Donadio, M. Parrinello, Canonical sampling through velocity rescaling, J. Chem. Phys. 126 (2007) 014101, https://doi.org/10.1063/1.2408420.

[31] T. Darden, D. York, L. Pedersen, Particle mesh Ewald: An $N \cdot \log(N)$ method for Ewald sums in large systems, J. Chem. Phys. 98 (1993) 10089–10092, https://doi.org/10.1063/1.464397.

[32] S. Kumar, J.M. Rosenberg, D. Bouzida, R.H. Swendsen, P.A. Kollman, THE weighted histogram analysis method for free-energy calculations on biomolecules. I. The method, J. Comput. Chem. 13 (1992) 1011–1021, https://doi.org/10.1002/jcc.540130812.

[33] N. Islam, A. Dihingia, P. Manna, T. Das, J. Kalita, H.P. Dekaboruah, B.K. Saikia, Environmental and toxicological assessment of nanodiamond-like materials derived from carbonaceous aerosols, Sci. Total Environ. 679 (2019) 209–220, https://doi.org/10.1016/j.scitotenv.2019.04.446.

[34] H. Hu, H. Guo, X. Yu, K. Naito, Q. Zhang, Surface modification and disaggregation of detonation nanodiamond particles with biodegradable polyurethane, Colloids Surf. A Physicochem. Eng. Asp. 563 (2019) 302–309, https://doi.org/10.1016/j.colsurfa.2018.12.023.

[35] B. Woodhams, L. Ansel-Bollepalli, J. Surmacki, H. Knowles, L. Maggini, M. De Volder, M. Atatüre, S. Bohndiek, Graphitic and oxidised high pressure high temperature (HPHT) nanodiamonds induce differential biological responses in breast cancer cell lines, Nanoscale 10 (2018) 12169–12179, https://doi.org/10.1039/C8NR02177E.

[36] R. Que, M. Shao, T. Chen, H. Xu, S. Wang, S.-T. Lee, Diamond nanoparticles with more surface functional groups obtained using carbon nanotubes as sources, J. Appl. Phys. 110 (2011) 054321, https://doi.org/10.1063/1.3636103.

[37] Z. Rezaeifar, Z. Es'haghi, G.H. Rounaghi, M. Chamsaz, Hyperbranched polyglycerol/graphene oxide nanocomposite reinforced hollow fiber solid/liquid phase microextraction for measurement of ibuprofen and naproxen in hair and waste water samples, J. Chromatogr. B 1029–1030 (2016) 81–87, https://doi.org/10.1016/j.jchromb.2016.07.010.

[38] E. Mohammadifar, V. Ahmadi, M.F. Gholami, A. Oehrl, O. Kolyvushko, C. Nie, I. S. Donskyi, S. Herziger, J. Radnik, K. Ludwig, C. Böttcher, J.P. Rabe, K. Osterrieder, W. Azab, R. Haag, M. Adeli, Graphene-assisted synthesis of 2D polyglycerols as innovative platforms for multivalent virus interactions, Adv. Funct. Mater. 31 (2021) 2009003, https://doi.org/10.1002/adfm.202009003.

[39] E. Roeven, L. Scheres, M.M.J. Smulders, H. Zuilhof, Design, synthesis, and characterization of fully Zwitterionic, functionalized dendrimers, ACS Omega 4 (2019) 3000–3011, https://doi.org/10.1021/acsomega.8b03521.

[40] A. Zielinski, M. Cieslik, M. Sobaszek, R. Bogdanowicz, K. Darowicki, J. Ryl, Multifrequency nanoscale impedance microscopy (m-NIM): A novel approach towards detection of selective and subtle modifications on the surface of polycrystalline boron-doped diamond electrodes, Ultramicroscopy 199 (2019) 34–45, https://doi.org/10.1016/j.ultramic.2019.01.004.

[41] F. Zhao, A. Vrajitoarea, Q. Jiang, X. Han, A. Chaudhary, J.O. Welch, R.B. Jackman, Graphene-nanodiamond heterostructures and their application to high current devices, Sci. Rep. 5 (2015) 13771, https://doi.org/10.1038/srep13771.

[42] B. Lesiak, L. Kövér, J. Tóth, J. Zemek, P. Jiricek, A. Kromka, N. Rangam, C sp2/sp3 hybridisations in carbon nanomaterials – XPS and (X)AES study, Appl. Surf. Sci. 452 (2018) 223–231, https://doi.org/10.1016/j.apsusc.2018.04.269.

[43] M. Cieślik, A. Susik, M. Banasiak, R. Bogdanowicz, K. Formela, J. Ryl, Tailoring diamondised nanocarbon-loaded poly(lactic acid) composites for highly electroactive surfaces: extrusion and characterisation of filaments for improved 3D-printed surfaces, Microchim. Acta 190 (2023) 370, https://doi.org/10.1007/s00604-023-05940-7.

[44] A. Kumar, C.K. Dixit, Methods for characterization of nanoparticles, in: advances in nanomedicine for the delivery of therapeutic nucleic acids, Elsevier, 2017: pp. 43–58. doi: 10.1016/B978-0-08-100557-6.00003-1.

[45] L. Ginés, S. Mandal, A.-I.-A. Ashek-I-Ahmed, C.-L. Cheng, M. Sow, O.A. Williams, Positive zeta potential of nanodiamonds, Nanoscale 9 (2017) 12549–12555, https://doi.org/10.1039/C7NR03200E.

MOST WIEDZY

[46] T. Yoshikawa, M. Liu, S.L.Y. Chang, I.C. Kuschnerus, Y. Makino, A. Tsurui, T. Mahiko, M. Nishikawa, Steric Interaction of Polyglycerol-Functionalized Detonation Nanodiamonds, Langmuir 38 (2022) 661–669, https://doi.org/10.1021/acs.langmuir.1c02283.
[47] Zetasizer Nano User Manual, Malvern Instruments Ltd., United Kingdom, 2012.
[48] H.-J. Butt, K. Graf, M. Kappl, Physics and chemistry of interfaces, Wiley-VCH, Weinheim, 2003.
[49] G.H. Lee, Y. Chang, T.-J. Kim, Characterization, in: Ultrasmall Lanthanide Oxide Nanoparticles for Biomedical Imaging and Therapy, Elsevier, 2014: pp. 43–67. doi: 10.1533/9780081000694.43.
[50] Y. Padrez, L. Golubewa, A. Bahdanava, M. Jankunec, I. Matulaitiene, D. Semenov, R. Karpicz, T. Kulahava, Y. Svirko, P. Kuzhir, Nanodiamond surface as a photoluminescent pH sensor, Nanotechnology 34 (2023) 195702, https://doi.org/10.1088/1361-6528/acb94b.
[51] P. Reineck, D.W.M. Lau, E.R. Wilson, N. Nunn, O.A. Shenderova, B.C. Gibson, Visible to near-IR fluorescence from single-digit detonation nanodiamonds: excitation wavelength and pH dependence, Sci. Rep. 8 (2018) 2478, https://doi.org/10.1038/s41598-018-20905-0.
[52] J. Xiao, P. Liu, L. Li, G. Yang, Fluorescence origin of nanodiamonds, J. Phys. Chem. C 119 (2015) 2239–2248, https://doi.org/10.1021/jp512188x.
[53] D.R. Lide, Chemical Rubber Company, eds., CRC handbook of chemistry and physics: a ready-reference book of chemical and physical data, 90. ed., 2009–2010, CRC Press, Boca Raton, FLa., 2009.
[54] P. Reineck, D.W.M. Lau, E.R. Wilson, K. Fox, M.R. Field, C. Deeleepojananan, V. N. Mochalin, B.C. Gibson, Effect of surface chemistry on the fluorescence of detonation nanodiamonds, ACS Nano 11 (2017) 10924–10934, https://doi.org/10.1021/acsnano.7b04647.
[55] G. Shenoy, J. Ettedgui, C. Mushti, J. Hong, K. Lane, B. Blackman, H.-S. Jung, Y. Takagi, Y. Seol, M. Brechbiel, R.E. Swenson, K.C. Neuman, General method to increase carboxylic acid content on nanodiamonds, Molecules 27 (2022) 736, https://doi.org/10.3390/molecules27030736.
[56] N. Nunn, N. Prabhakar, P. Reineck, V. Magidson, E. Kamiya, W.F. Heinz, M. D. Torelli, J. Rosenholm, A. Zaitsev, O. Shenderova, Brilliant blue, green, yellow, and red fluorescent diamond particles: synthesis, characterization, and multiplex imaging demonstrations, Nanoscale 11 (2019) 11584–11595, https://doi.org/10.1039/C9NR02593F.
[57] Y. Luo, C.M. Breeding, Fluorescence produced by optical defects in diamond: measurement, characterization, and challenges, g&g 49 (2013) 82–97, https://doi.org/10.5741/GEMS.49.2.82.
[58] T.-H. Tsai, U.F.S. D'Haenens-Johansson, Rapid gemstone screening and identification using fluorescence spectroscopy, Appl. Opt. 60 (2021) 3412, https://doi.org/10.1364/AO.419885.
[59] S. Chauhan, N. Jain, U. Nagaich, Nanodiamonds with powerful ability for drug delivery and biomedical applications: Recent updates on in vivo study and patents, J. Pharm. Anal. 10 (2020) 1–12, https://doi.org/10.1016/j.jpha.2019.09.003.
[60] A. Saadati, M. Hasanzadeh, F. Seidi, Biomedical application of hyperbranched polymers: Recent Advances and challenges, TrAC Trends Anal. Chem. 142 (2021) 116308, https://doi.org/10.1016/j.trac.2021.116308.
[61] B. Xiang, Y. Xue, Z. Liu, J. Tian, H. Frey, Y. Gao, W. Zhang, Water-soluble hyperbranched polyglycerol photosensitizer for enhanced photodynamic therapy, Polym. Chem. 11 (2020) 3913–3921, https://doi.org/10.1039/D0PY00431F.
[62] M. Tully, M. Dimde, C. Weise, P. Pouyan, K. Licha, M. Schirner, R. Haag, Polyglycerol for Half-Life Extension of Proteins—Alternative to PEGylation? Biomacromolecules 22 (2021) 1406–1416, https://doi.org/10.1021/acs.biomac.0c01627.
[63] M. Rahman, M. Alrobaian, W.H. Almalki, M.H. Mahnashi, B.A. Alyami, A. O. Alqarni, Y.S. Alqahtani, K.S. Alharbi, S. Alghamdi, S.K. Panda, A. Fransis, A. Hafeez, S. Beg, Superbranched polyglycerol nanostructures as drug delivery and theranostics tools for cancer treatment, Drug Discov. Today 26 (2021) 1006–1017, https://doi.org/10.1016/j.drudis.2020.11.007.
[64] M. Elstner, D. Porezag, G. Jungnickel, J. Elsner, M. Haugk, Th. Frauenheim, S. Suhai, G. Seifert, Self-consistent-charge density-functional tight-binding method for simulations of complex materials properties, Phys. Rev. B 58 (1998) 7260–7268, https://doi.org/10.1103/PhysRevB.58.7260.
[65] T.A. Niehaus, M. Elstner, Th. Frauenheim, S. Suhai, Application of an approximate density-functional method to sulfur containing compounds, J. Mol. Struct.: THEOCHEM 541 (2001) 185–194, https://doi.org/10.1016/S0166-1280(00)00762-4.
[66] M. Gaus, Q. Cui, M. Elstner, DFTB3: Extension of the self-consistent-charge density-functional tight-binding method (SCC-DFTB), J. Chem. Theory Comput. 7 (2011) 931–948, https://doi.org/10.1021/ct100684s.
[67] A.K. Rappe, C.J. Casewit, K.S. Colwell, W.A. Goddard, W.M. Skiff, UFF, a full periodic table force field for molecular mechanics and molecular dynamics simulations, J. Am. Chem. Soc. 114 (1992) 10024–10035, https://doi.org/10.1021/ja00051a040.

MOST WIEDZY